PERGAMON

International Journal of Multiphase Flow 27 (2001) 477–526

International Journal of Multiphase Flow

www.elsevier.com/locate/ijmulflow

Binary two-phase flow with phase change in porous media

S. Békri[a], O. Vizika[b], J.-F. Thovert[c], P.M. Adler[a,*]

[a] *IPGP, Tour 24, 2ème étage, 75252 Paris Cedex 05, France*
[b] *2IFP, BP 311, 92256 Rueil-Malmaison Cedex, France*
[c] *PTM/LCD, BP 179, 86960 Futuroscope Cedex, France*

Received 20 April 1999; received in revised form 11 April 2000

Abstract

Flow of multicomponent mixtures with interphase mass transfer through porous media has been analyzed by combining thermodynamics of real fluids, the use of immiscible Boltzmann code and reconstructed porous media. A general algorithm is detailed and applied for comparison with Poiseuille flow where a semi-analytical solution can be found. A series of structures and phenomena are then analysed; attention is mostly focused on liquid to gas transition (or vaporization) and retrograde condensation; phase distribution and macroscopic quantities such as composition, liquid saturation and pressure evolution are systematically plotted. The role of the location of nucleation sites is shortly investigated with a periodically constricted tube. The total mass flow rate influenced the phase distribution and circulation in a two-dimensional network. Finally, relative permeabilities of a reconstructed medium are discussed; an interesting feature is that they follow hysteresis cycles for retrograde condensation.

Keywords: Porous media; Two-phase flow; Phase change; Lattice Boltzmann method; Reconstructed media; Peng–Robinson equation

1. Introduction

The general objective of this work which was primarily motivated by the oil industry, is to describe the flow of two-component mixtures through porous media when phase changes occur. When pressure goes down, two typical evolutions may happen, which are liquid

* Corresponding author.

0301-9322/01/$ - see front matter
PII: S0301-9322(00)00034-3

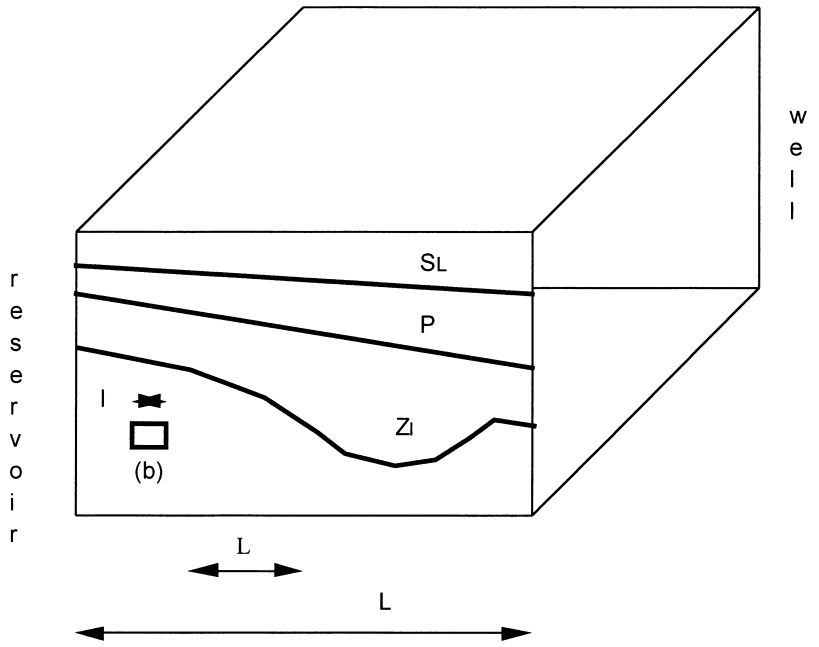

(a)

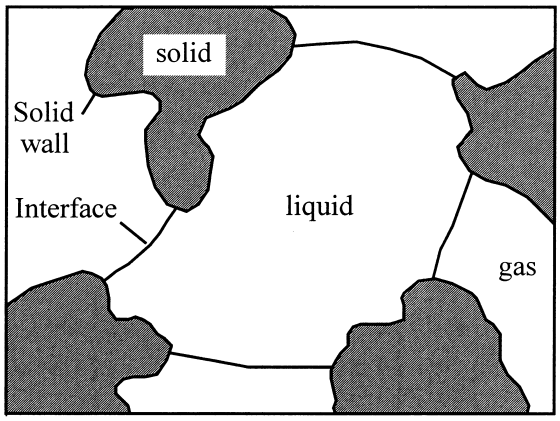

(b)

Fig. 1. Liquid vaporization in a three-dimensional porous medium. (a) View of the reservoir at the large scale; (b) the porous medium at the pore scale.

vaporization (LV) and retrograde condensation (RC); these two cases will be denoted by their initials LV and RC; LV is tentatively illustrated in Fig. 1. The mixture is characterized by its pressure, temperature and composition at the origin $x = 0$, representing the conditions in an oil reservoir. The flow is characterized by the global mass flux Q. The mixture in the reservoir may be in the form of either one- (liquid or vapor) or two-phase. Besides, pressure variations due to the flow may induce condensation or vaporization and composition changes. One wishes to predict, as functions of the mass flux and of the reservoir conditions, the longitudinal profiles of the various quantities of interest and particularly of the pressure, gas/liquid saturation and mixture composition.

This important topic has received some attention in the literature, but with different points of view. First, detailed thermodynamic properties are known and used for the analysis of static properties (Reid et al., 1987; Gravier, 1986); moreover, theoretical analyses of dynamic properties of mixtures have been developed (Atkin and Craine, 1976a, 1976b), but without any application to real cases. The closest field to the present study is foamy oil which has been recently reviewed by Sheng et al. (1999) in the special issue Hayes and Maini (1999). There are a number of recent works, both theoretical and experimental. Some of them focus on the aspects such as nucleation which are physically important, but are not within the main scope of this work. Li and Yortsos (1995) and Du and Yortsos (1999) studied capillary networks, both experimentally and numerically. In a slightly different study, El Yousfi et al. (1991) observed bubble formation during pressure decline in a transparent micromodel, but there is no global flow motion in this experiment. In our case, as in Geilikman and Dusseaut (1999), the pressure variations are induced by the flow itself.

The major purpose of this work is to determine the macroscopic evolution at the reservoir scale L of a binary mixture at a given mass flow rate based on a microscopic description of what is going on at the pore scale l. It is assumed that l is much smaller than L. It should be noted that the components, pressure and temperature conditions are chosen in order to be representative of a typical oil reservoir.

Two additional fundamental hypotheses are necessary. First, the longitudinal variations of all the quantities take place over distances $\mathscr{L}$, much larger than the characteristic pore size l and much smaller than the reservoir length L; to summarize

$$l \ll \mathscr{L} \ll L \tag{1}$$

Second, because of the local motions and of diffusion, each phase is assumed to be well mixed and the concentration of a given component is constant in a given phase at the local scale 1; we shall describe this second assumption in Section 2.4.

This paper is organized as follows. In Section 2, after some notational definitions, the thermodynamics of a multiphase, multicomponent mixture are given in detail; the determination of material properties such as viscosities and surface tension is schematized. The motion of each phase is computed with a classical Immiscible Lattice Boltzmann (ILB) code, which was originated by Gustensen (1992) and applied by Ginzbourg and Adler (1995). Finally, realistic samples of porous media can be obtained by the technique of reconstructed media (Adler et al., 1990) which is briefly recalled.

Section 3 provides some numerical informations on the actual implementation of the general code. The algorithmic structure of the ILB code is first presented. Then the Flash code is

introduced; based on the thermodynamic properties, it determines the liquid saturation when temperature, pressure and composition of the mixture are known; by the same token, the partition coefficients and the necessary physical properties are also calculated. Finally, the general algorithm which combines all the previous ingredients as subroutines, is explained in detail; it predicts all the characteristics of the flow for a given saturation.

Due to the complex structure of this algorithm, it was necessary to check it against results obtained by independent means in a simple configuration. This is done in Section 4 for a plane Poiseuille flow where the velocity profile is simply a combination of parabolic profiles. The agreement between various versions of the code is generally excellent both for LV and RC.

Section 5 is devoted to the study of several different configurations. One started with two-dimensional structures where the evolution of the phase distribution can be easily graped. A periodic constriction provides a good example to the analysis of the influence of the location of nucleation in the evolution of such mixtures; it will be seen that especially for RC, this influence is drastic. Then the magnitude of the global mass flow rate is varied and analysed for a two-dimensional network; when flow is large, the gas phase is seen to break through the whole network, pushing the liquid phase in the transversal channels where the velocities are small. Finally, reconstructed media are addressed; because of the uneasy visualisation, results are only discussed by means of macroscopic quantities; relative permeabilities are also systematically computed at various stages of the evolution; the influence of the total mass flow rate is clearly seen on these overall results and liquid permeability is considerably diminished when mass flow rate is increased; this confirms the visual findings obtained for two-dimensional networks. For RC permeabilities are found to go along hysteresis cycles.

Some remarks are presented in Section 6, and some extensions of the present work are proposed.

2. General

In this section, a few notations are introduced first. Then the thermodynamic properties and the constitutive equations are presented. The algorithm of the ILB code is summarized. Finally, the technique of reconstructed media is presented.

2.1. Notations

Apart from the pressure P and the temperature T, a two-phase two-component mixture is characterised by its composition. As a general rule, quantities associated with a component or with a phase are denoted by a subscript ($\alpha = 1$ or 2) or a superscript ($\beta = \mathrm{L}$ or V, for liquid or vapor), respectively. Accordingly, z_α denotes the global molar fraction of component α, X_α or X_α^{L} the mole fraction of component α in the liquid, Y_α or X_α^{V}, the mole fraction of component α in the vapor. The partition coefficient K_α is defined as the ratio at equilibrium

$$K_\alpha = Y_\alpha / X_\alpha \tag{2}$$

Each component is also characterised by its molar mass M_α, and its molar volume within each phase V_α^β. The number of moles of component α in phase β is denoted by N_α^β. In addition,

$$N^{\beta} = N_1^{\beta} + N_2^{\beta}$$

$$N_{\alpha} = N_{\alpha}^{\mathrm{L}} + N_{\alpha}^{\mathrm{V}}$$

$$N = N^{\mathrm{L}} + N^{\mathrm{V}} \tag{3}$$

It may be shown that for any α

$$\frac{N^{\mathrm{L}}}{N} = \frac{Y_{\alpha} - z_{\alpha}}{Y_{\alpha} - X_{\alpha}} \quad \frac{N^{\mathrm{V}}}{N} = \frac{z_{\alpha} - X_{\alpha}}{Y_{\alpha} - X_{\alpha}} \quad \frac{N^{\mathrm{V}}}{N^{\mathrm{L}}} = \frac{z_{\alpha} - X_{\alpha}}{Y_{\alpha} - z_{\alpha}} \tag{4}$$

The definitions above are true for any number of components, without impairing Eq. (4). However, for binary mixtures, it can be deduced from Eqs. (2) and (4) that

$$X_1 = \frac{1 - K_2}{K_1 - K_2} \quad X_2 = \frac{K_1 - 1}{K_1 - K_2}$$

$$Y_1 = K_1 \frac{1 - K_2}{K_1 - K_2} \quad Y_2 = K_2 \frac{K_1 - 1}{K_1 - K_2} \tag{5}$$

Note that, the condition $0 \leq X_{\alpha}^{\beta} \leq 1$ implies

$$K_1 \leq 1 \leq K_2 \quad \text{or} \quad K_2 \leq 1 \leq K_1 \tag{6}$$

Moreover, Eqs. (4) and (5) imply that

$$\frac{N^{\mathrm{L}}}{N^{\mathrm{V}}} = K_1 K_2 \frac{\left(\frac{z_1}{K_1} + \frac{z_2}{K_2}\right) - 1}{(z_1 K_1 + z_2 K_2) - 1} \tag{7}$$

In order to write the transport equations, which result from mass and momentum balances, introduce the densities of each component within each phase

$$\rho_{\alpha}^{\beta} = M_{\alpha} / V_{\alpha}^{\beta} \tag{8}$$

and the phase densities

$$\rho^{\beta} = \rho_1^{\beta} + \rho_2^{\beta} \tag{9}$$

Finally, let us introduce a few dynamical quantities. The phase viscosities are denoted by μ^{β}; the viscosity ratio m is defined as

$$m = \frac{\mu^{\mathrm{V}}}{\mu^{\mathrm{L}}} \tag{10}$$

The mass fluxes are denoted in the following way. Q, Q^{β} and q_{α} are the global mass flux, the mass flux per phase and the mass flux per component, respectively. The partial mass fluxes $\overline{q_{\alpha}}$ are defined as

$$\overline{q_\alpha} = \frac{q_\alpha}{q_1 + q_2} \tag{11}$$

2.2. Thermodynamical equations

2.2.1. Equation of state

In the vapor phase, the pressure P^{V}, temperature T^{V} and molar volume V^{V} are related by an equation of state, which accounts for the non-ideality of the gas, via its compressibility factor Z

$$Z = \frac{P^{\mathrm{V}} V^{\mathrm{V}}}{R T^{\mathrm{V}}} \tag{12}$$

where R is the perfect gas constant (8314 J/mol/K). Among the numerous models proposed in the literature (cf. Atkin and Craine, 1976a, 1976b; Reid et al., 1987), one of the most successful is the Peng–Robinson equation, which belongs to the class of "cubic equations of state". For a single component gas, it can be cast into

$$P^{\mathrm{V}} = \frac{R T^{\mathrm{V}}}{V^{\mathrm{V}} - b} - \frac{a}{V^{\mathrm{V}}(V^{\mathrm{V}} - b) + b(V^{\mathrm{V}} - b)} \tag{13a}$$

or equivalently,

$$Z^3 - (1 - B)Z^2 + (A - 3B^2 - 2B)Z + \left(B^2 - AB + B^3\right) = 0 \tag{13b}$$

where

$$A = \frac{aP}{(RT)^2} \quad B = \frac{bP}{RT}$$

$$a = a_0 R^2 \Omega^2 \quad b = b_0 M R$$

$$\Omega^2 = \frac{\left[1 + f\omega\left(1 - \sqrt{T/T_{\mathrm{c}}}\right)\right]^2 T_{\mathrm{c}}^2}{P_{\mathrm{c}}} \quad M = \frac{T_{\mathrm{c}}}{P_{\mathrm{c}}} \tag{14}$$

P_{c} and T_{c} are the critical pressure and temperature of the gas, ω is the acentric factor, and the constants are fitted to match experimental data. For hydrocarbons (see Reid et al., 1987; Section 3.6),

$$a_0 = 0.45724$$

$$b_0 = 0.07780$$

$$f_\omega = 0.37464 + 1.54226\omega - 0.26992\omega^2 \tag{15}$$

For binary gas mixtures, the Peng–Robinson equation of state, Eqs. (13a) and (13b), are

supposed to apply. However, the coefficients A and B are now defined by a mixing rule (Reid et al., 1987; Section 8.12)

$$A = \frac{aP}{(RT)^2} \quad B = \frac{Pb}{RT}$$

$$a = \sum_{\alpha=1}^{2}\sum_{\alpha'=1}^{2} Y_\alpha Y_{\alpha'}(1 - C_{\alpha\alpha'})\sqrt{a_\alpha a_{\alpha'}} \quad b = \sum_{\alpha=1}^{2} Y_\alpha b_\alpha \tag{16}$$

where a_α and b_α are defined by Eq. (14) for the component α; Y_α is the molar fraction of component α, and $C_{\alpha\alpha'}$ is a binary interaction parameter. For mixtures of hydrocarbons, $C_{\alpha\alpha'}$ is usually taken as zero (Gravier, 1986).

2.2.2. Equilibrium conditions between liquid and vapor phases

The equilibrium at the interface is ruled by the condition of equality of the chemical potentials μ_α^β in both phases for the two components; they can be expressed in term of the fugacities f_α^β, with respect to a reference state (subscript 0)

$$\mu_\alpha^\beta = \mu_{\alpha_0}^\beta + RT \ln \frac{f_\alpha^\beta}{f_{\alpha 0}^\beta} \tag{17}$$

The fugacity coefficient Φ_α^β is defined by

$$f_\alpha^\beta = \Phi_\alpha^\beta X_\alpha^\beta P_\alpha \tag{18}$$

Hence, the equilibrium condition becomes

$$\frac{Y_\alpha}{X_\alpha} = \frac{\Phi_\alpha^{\mathrm{L}} P^{\mathrm{L}}}{\Phi_\alpha^{\mathrm{V}} P^{\mathrm{V}}} = K_\alpha \tag{19}$$

Note that if the interface curvature is ignored, $P^{\mathrm{L}} = P^{\mathrm{V}}$.

The partition coefficients K_α depend upon pressure, temperature, and composition of the mixture. They can be evaluated by introducing the equation of state into the general expression of the fugacity coefficient (Reid et al., 1987; Section 8.12)

$$RT^\beta \ln \Phi_\alpha^\beta = \int_{V^\beta}^{\infty} \left[\left(\frac{\partial P^\beta}{\partial n_\alpha^\beta} \right)_{T^\beta V n'_\alpha \beta} - \frac{RT^\beta}{V} \right] \mathrm{d}V - RT^\beta \ln Z^\beta \tag{20}$$

Recall that Z is the compressibility factor, Eq. (12). If a cubic equation of state is used in Eq. (20), the explicit expression for the fugacity coefficient becomes (see Reid et al., 1987; Table 5.13)

$$\ln \Phi_\alpha^\beta = \frac{b_\alpha}{b^\beta}(Z^\beta - 1) - \ln(Z^\beta - B^\beta)$$

$$+\frac{A^\beta}{B^\beta\sqrt{u^2-4w}}\left(\frac{b_\alpha}{b^\beta}-\delta_\alpha^\beta\right)\ln\frac{2Z^\beta+B^\beta\left(u+\sqrt{u^2-4w}\right)}{2Z^\beta+B^\beta\left(u-\sqrt{u^2-4w}\right)} \tag{21}$$

For the specific case of the Peng–Robinson equation, with zero interaction coefficients,

$$u=2 \quad w=-1 \quad \frac{b_\alpha}{b^\beta}=\frac{T_{c\alpha}/P_{c\alpha}}{\sum_\alpha X_\alpha^\beta T_{c\alpha}/P_{c\alpha}} \quad \delta_\alpha^\beta=2\sqrt{\frac{a_\alpha^\beta}{b^\beta}} \tag{22}$$

The partition coefficients K_α can be obtained from the combination of Eqs. (19) and (21).

2.2.3. Other constitutive equations: viscosities and surface tension

2.2.3.1. Liquid mixture viscosity. The viscosity μ_m^L of the liquid phase is obtained by the mixing rule of Teja and Rice (Reid et al., 1987; Section 9.13). It involves the critical coefficients of each component, and their viscosities in some reference state. These were evaluated by Letsou and Stiel model (Reid et al., 1987; Section 9.12) which again makes use only of universal constants and of the critical temperatures.

These formulae can be summarized as follows. The viscosity of the liquid mixture is given by

$$\ln\left(\mu_m^L\varepsilon_m\right)=\ln\left(\mu^L\varepsilon\right)^{(r1)}+\left[\ln\left(\mu^L\varepsilon\right)^{(r2)}-\ln\left(\mu^L\varepsilon\right)^{(r1)}\right]\frac{\omega_m-\omega^{(r1)}}{\omega^{(r2)}-\omega^{(r1)}} \tag{23}$$

where the superscripts (r1) and (r2) refer to two reference fluids. μ^L is the viscosity, ω is the acentric factor and ε is a parameter defined as

$$\varepsilon=\frac{V_c^{\frac{2}{3}}}{(T_cM)^{\frac{1}{2}}} \tag{24}$$

Composition is introduced in the definitions of ω_m, V_{cm}, T_{cm} and M_m. The rules to compute these mixtures parameters are

$$\begin{gathered}V_{cm}=\sum_\alpha\sum_\gamma X_\alpha X_\gamma V_{c\alpha\gamma} \qquad T_{cm}=\frac{\sum_\alpha\sum_\gamma X_\alpha X_\gamma T_{c\alpha\gamma}V_{c\alpha\gamma}}{V_{cm}} \qquad M_m=\sum_\alpha X_\alpha M_\alpha \\ \omega_m=\sum_\alpha X_\alpha\omega_\alpha \qquad V_{c\alpha\gamma}=\frac{\left(V_{c\alpha}^{\frac{1}{3}}+V_{c\gamma}^{\frac{1}{3}}\right)}{8} \qquad T_{c\alpha\gamma}V_{c\alpha\gamma}=\psi_{\alpha\gamma}\left(T_{c\alpha}T_{c\gamma}V_{c\alpha}V_{c\gamma}\right)^{\frac{1}{2}}\end{gathered} \tag{25}$$

where $\psi_{\alpha\gamma}$ is an interaction parameter of order unity which must be found from experimental data.

It is important to note that in Eq. (23) the viscosity values $\mu^{(r1)}$ and $\mu^{(r2)}$ for the two

reference fluids are to be obtained at temperatures $T(T_c^{(r1)}/T_{cm})$ and $T(T_c^{(r2)}/T_{cm})$, respectively; T is the temperature of the mixture.

As the reference fluids (r1) and (r2) may be chosen as different from the actual components in the mixture, it is normally advantageous to select them from the principal components in the mixture. Letsou and Stiel (Reid et al., 1987; Section 9.12) proposed for saturated liquids

$$\mu_{SL}\xi = (\mu_L\xi)^{(0)} + \omega(\mu_L\xi)^{(1)} \tag{26}$$

where the parameters $(\mu_L\xi)^{(0)}$ and $(\mu_L\xi)^{(1)}$ are functions only of reduced temperature and ξ

$$(\mu_L\xi)^{(0)} = 10^{-3}(2.648 - 3.725T_r + 1.309T_r^2)$$

$$(\mu_L\xi)^{(1)} = 10^{-3}(7.425 - 13.39T_r + 5.933T_r^2) \tag{27}$$

The units have been converted to yield μ_{SL} in centipoises even though ξ has the dimensions of micropoises

$$\xi = 0.176\left(\frac{T_c}{M^3P_c^4}\right)^{\frac{1}{6}} \tag{28}$$

2.2.3.2. Gas mixture viscosity. The viscosity μ^V of the vapor phase is evaluated using Lucas method, adapted for gas mixtures (Reid et al., 1987; Section 9.7). It is a rather complex model, but unlike many others it does not require to provide estimates of the low-pressure, viscosity or any additional quantity attached to the components. It makes use only of a few universal numerical constants and of the critical temperature and pressures of the species which are given in Table 1.

For the reduced temperature of interest, calculate a parameter Z_1

$$Z_1 = \left[0.807\ T_r^{0.618} - 0.357\exp(-0.449\ T_r) + 0.340\exp(-4.058\ T_r) + 0.018\right]$$

$$Z_2 = \left[1 + \frac{aP_r^e}{bP_r^f + (1 + cP_r^d)^{-1}}\right]Z_1$$

Table 1
Some thermodynamic coefficients for the various components of practical interest (cf. Reid et al., 1987)

Component i	$[P_i]$	M (g/mol)	σ (Å)	ε/K	V_c (cm^3/mol)
CO2	78.0	44.01	3.941	195.2	94.16
C1	77.0	16.04	3.758	148.6	98.99
N2	41.0	28.013	3.798	71.4	90.20
C3	150.3	99.097	5.118	237.1	202.85
C5	225.0	72.151	5.784	341.1	305.92

$$a = \frac{a_1}{T_r}\exp a_2 T_r^{\gamma} \quad b = a(b_1 T_r - b_2) \quad c = \frac{c_1}{T_r}\exp c_2 T_r^{\delta}$$

$$d = \frac{d_1}{T_r}\exp d_2 T_r^{\varepsilon} \quad e = 1.3088 \quad f = f_1 \exp f_2 T_r \xi$$

$$\begin{array}{lll} a_1 = 1.245 \times 10^{-3} & a_2 = 5.1726 & \gamma = -0.3286 \\ b_1 = 1.6553 & b_2 = 1.2723 & \\ c_1 = 0.4489 & c_2 = 3.0578 & \delta = -37.7332 \\ d_1 = 1.7368 & d_2 = 2.2310 & \varepsilon = -7.6351 \\ f_1 = 0.9425 & f_2 = -0.1853 & \zeta = 0.4489 \end{array} \tag{29}$$

Finally, the dense gas viscosity is calculated as

$$\mu^{V} = \frac{Z_2}{\xi} \tag{30}$$

2.2.3.3. Surface tension. The surface tension σ, which is required in complex geometries, is estimated using McLeod–Sugden correlation (Reid et al., 1987; Section 12.5). It makes use of the so-called parachor coefficients for each component, which have to be provided

$$\sigma^{\frac{1}{4}} = \sum_{\alpha=1}^{n} [P_\alpha]\left(\frac{X_\alpha}{V^{L}} - \frac{Y_\alpha}{V^{G}}\right) \tag{31}$$

where $[P_\alpha]$ is the parachor of component α. This coefficient is given in Table 1.

2.3. Reconstructed media

First, let us briefly describe the typical measurements which are fully reported by Adler et al. (1990). Consider the thin section displayed in Fig. 2(a). At each point $\mathbf{x}$ within the sample, one can define a phase function $Z(\mathbf{x})$

$$Z(\mathbf{x}) = \begin{cases} 1 & \text{if } \mathbf{x} \text{ belongs to the pore space} \\ 0 & \text{otherwise} \end{cases}. \tag{32a}$$

$Z(\mathbf{x})$ can be determined by image analysis and stored as a numerical file. Then, the porosity is computed according to

$$\varepsilon = \overline{Z(\mathbf{x})} \tag{32b}$$

The other important quantity is the second moment of the phase function which is also called the correlation function

$$R_Z(u) = \overline{\left[Z(\mathbf{x}) - \varepsilon\right] \cdot \left[Z(\mathbf{x}+\mathbf{u}) - \varepsilon\right]}/(\varepsilon - \varepsilon^2) \tag{32c}$$

where $u = \|\mathbf{u}\|$.

These measurements are usually performed in a single, but otherwise arbitrary, plane since most materials are isotropic at the small scale. An example of such a correlation function is

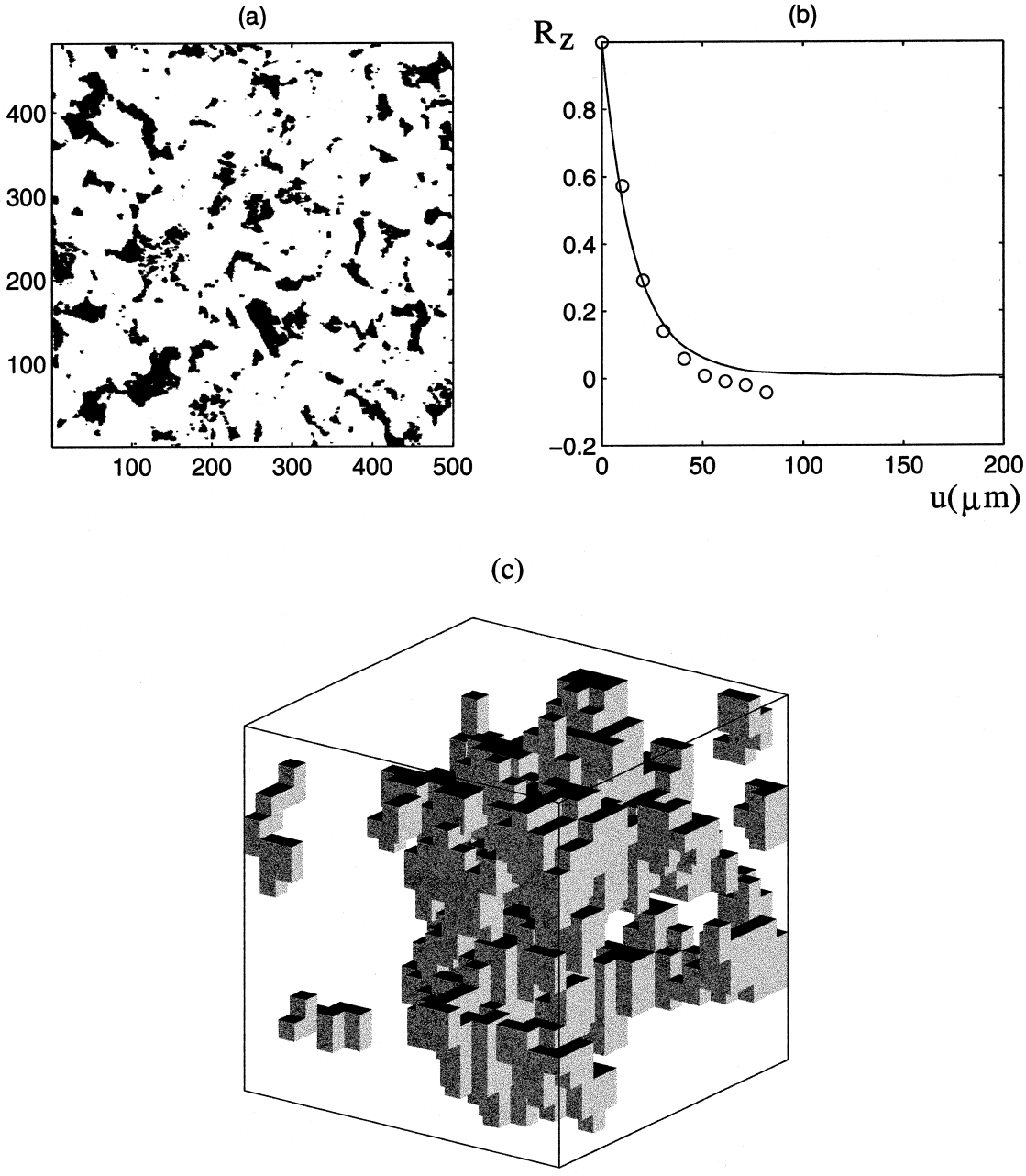

Fig. 2. Reconstruction of three-dimensional porous media. (a) Binarized thin section of dimensions $12.2 \times 12.2\ \mu m^2$. The porosity is equal to 0.157. (b) The correlation function as a function of the lag u; the solid line corresponds to the experimental data and '○' corresponds to the reconstructed sample. (c) The reconstructed piece of porous medium with the measured porosity and the measured correlation function; the solid phase is grey.

displayed in Fig. 2(b). Porous media with the same experimental porosity and correlation function can be generated by a statistical procedure which is given in detail in Adler et al. (1990).

For practical purposes only, the porous medium is constructed in a discrete manner. It is considered as being composed of N_c^3 small cubes, each of the same size a. These elementary cubes are filled either with liquid, or with solid. An additional condition is imposed by the fact that the sample of generated porous medium has a finite size $N_c a$. In such a case, it is standard to consider periodic boundary conditions on the sample for the determination of permeability (cf. Adler et al., 1990). The same requirement should be imposed on the generation of the medium itself. An example is displayed in Fig. 2(c).

It might be useful to relate the size of the unit cell to the scales which were introduced by Eq. (1). $N_c a$ is assumed to be large with respect to the pore scale l, so that the sample is representative of the porous medium. However, $N_c a$ is supposed to be small with respect to $\mathscr{L}$

$$l \ll N_c a \tag{33a}$$

2.4. Transport equations: the lattice Boltzmann model

All the fluid properties, namely composition, viscosity and density, are assumed to be constant in each phase at the local scale; the phase properties can be calculated at thermodynamic equilibrium. This is fulfilled when two assumptions are verified. First, the size of the unit cell is supposed to be small with respect to $\mathscr{L}$, the length scale over which significant changes occur. To summarize,

$$N_c a << \mathscr{L} \tag{33b}$$

Second, because of diffusive and convective effects, the phases are supposed to be well mixed at the pore level. Note that more generally, conditions (33a) and (33b) hold for all the spatially periodic media that are going to be studied.

The transport equations reduce to the global mass and momentum balances. They can be written in the form of Navier–Stokes equations. However, because of the multiphase character of the flow, the ILB algorithm is used.

During the last few years, numerous models based on single phase *Lattice Gas* (LG) and *Lattice Boltzmann* (LB) models have been developed. They originated in the FHP two-dimensional LG automaton introduced by Frisch et al. (1986, 1987) and in the FCHC four-dimensional LG developed by D'Humières et al. (1986) for simulations in three-dimensions. The assumption of molecular chaos is made in LB models suggested by McNamara and Zanetti (1988) and developed by Higuera and Jimenez (1989). Incompressible Navier–Stokes equations are recovered by both approaches in an asymptotic limit.

Some of these single phase methods have been extended to simulate the behaviour of two or more immiscible fluids. ILB multiphase models are developed on the basis of the single phase LB models and ILG models; they consist of Boltzmann equations supplemented by perturbation of populations near the interface in order to introduce surface tension; the separation of phases is performed in the same manner as in ILG models.

Let us briefly present the two immiscible two-phase three-dimensional models with rest

populations which are going to be used. The interface is defined as the set of nodes where the two phases are simultaneously present. The first model does not provide any new procedure, since it was already developed by Gustensen (1992), but the possibility to have different viscosities as well as different numbers of rest populations is formally incorporated into it; at the interface where both populations are present, the collision matrix is chosen by the majority rule. Hence, the choice of the collision matrix is ambiguous at the nodes where the red mass is equal to the blue one. The second model is the same in bulk, but a special collision matrix is introduced at the interface in order to satisfy the standard interfacial conditions at first order.

We have not used the more sophisticated version of Appert and Zaleski (1990) because it would have necessitated a much more sophisticated version which would have been a study in itself. Moreover, the equation of state is not as flexible as we wished. Hence, we choose this intermediate situation.

The algorithm which corresponds to these models is detailed in Section 3.

3. Numerical algorithms

3.1. Lattice Boltzmann code

This algorithm is essentially the same as the one described in Ginzbourg and Adler (1995) to which the reader is referred for further details.

Let the populations of red or blue phase of velocity $\mathbf{C}_i$ be $N_i^{\mathrm{R}}(\mathbf{r}, t)$ or $N_i^{\mathrm{B}}(\mathbf{r}, t)$, $(i = 0, \ldots, b_{\mathrm{m}} = 24)$, respectively. The index 0 corresponds to rest of the populations; the numbers of rest populations are L^{R} or L^{B} for red or blue phase, respectively; the moving populations may have $b_{\mathrm{m}} = 24$ velocities $\mathbf{C}_i$ in the FCHC model. The algorithm consists of the following five steps.

Step 1 (Definition of the fields at time t).

1.1. Calculation of the densities of each phase ρ_{R}, ρ_{B}

$$\rho_K(\mathbf{r}, t) = \sum_{i=0}^{24} N^K(\mathbf{r}, t) W_i^K,\ W_0^{\mathrm{K}} = L^K,\ W_i^K = 1, \quad i, \ldots, 24 \text{ for } K = \mathrm{R}, \mathrm{B} \tag{34a}$$

1.2. Calculation of the total population N_i and of the total density

$$N_i(\mathbf{r}, t) W_i = N_i^{\mathrm{R}} W_i^{\mathrm{R}} + N_i^{\mathrm{B}}(\mathbf{r}, t) W_i^{\mathrm{B}}, \quad i = 0, \ldots, 24$$

$$W_0 = L,\ W_i^K = 1, \quad i = 1, \ldots, 24$$

$$\rho(\mathbf{r}, t) = \rho_{\mathrm{R}}(\mathbf{r}, t) + \rho_{\mathrm{B}}(\mathbf{r}, t) \tag{34b}$$

1.3. Addition of external forces $\mathbf{F}^{\mathrm{R}}$ and $\mathbf{F}^{\mathrm{B}}$ according to the single phase algorithm of Succi et al. (1989) (expressions for these forces will be given at the end of this subsection)

$$N_i'(\mathbf{r},t) = N_i(\mathbf{r},t) + \delta N_i^F(\mathbf{r},t);\ \delta N_i^F(\mathbf{r},t) = \frac{D}{c^2 b_{\mathrm{m}}}\rho(\mathbf{r},t)\big(\mathbf{F}(\mathbf{r},t)\cdot\mathbf{C}_i\big),\quad D=4,\ \forall i$$
$$c^2 = (\mathbf{C}_i\cdot\mathbf{C}_i)\overset{\mathrm{FCHC}}{\equiv}2, \tag{34c}$$

where the expression of $\mathbf{F}(\mathbf{r},t)$ depends upon the chosen model:

- *Model 1: by majority of colors*

$$\mathbf{F}(\mathbf{r},t) = \mathbf{F}^{\mathrm{R}},\quad \rho_{\mathrm{B}}(\boldsymbol{r},t) < \rho_{\mathrm{R}}(\mathbf{r},t)$$
$$\mathbf{F}^{\mathrm{B}},\quad \rho_{\mathrm{B}}(\mathbf{r},t) > \rho_{\mathrm{R}}(\mathbf{r},t) \tag{34d}$$

- *Model 2:*

$$\mathbf{F}(\mathbf{r},t) = \frac{\mathbf{F}^{\mathrm{R}}\rho_{\mathrm{R}}(\mathbf{r},t) + \mathbf{F}^{\mathrm{B}}\rho_{\mathrm{B}}(\mathbf{r},t)}{\rho(\mathbf{r},t)} \tag{34e}$$

1.4. Calculation of the total velocity $\mathbf{u}$

$$\mathbf{u}(\mathbf{r},t) = \frac{\sum_{i=1}^{24} N_i'(\mathbf{r},t)\mathbf{C}_i}{\rho(\mathbf{r},t)} - \frac{1}{2}\mathbf{F}(\mathbf{r},t) \tag{34f}$$

Addition of $\{-\frac{1}{2}\mathbf{F}\}$ to the classical velocity expression is caused by the presence of the term $N_i^F(\mathbf{r},t)$ given by Eq. (34c) in LB equation. Defined in such a manner, the velocity $\mathbf{u}(\mathbf{r},t)$ corresponds to the local velocity in the equilibrium solutions for populations and, consequently, to the macroscopic velocity of the simulated fluid.

Step 2 (Collision of total populations)**.**

$$N_i^*(\mathbf{r},t) = N_i'(\mathbf{r},t) + \sum_{j=0}^{24} \boldsymbol{A}_{ij} N_j^{n\mathrm{eq}}(\mathbf{r},t) W_j,\quad i=0,\ldots,24$$
$$N_i^{n\mathrm{eq}} = N_i' - N_i^{\mathrm{eq}};\quad W_0 = L,\quad W_i = 1,\quad i=1,\ldots,24, \tag{35a}$$

where the equilibrium solution $\mathbf{N}^{\mathrm{eq}}$ is known. The collision operator $\mathbf{A}(\mathbf{r},t)$ and the number of rest populations $L(\mathbf{r},t)$ are different in Models 1 and 2; the coefficients of the collision matrices are related to the physical properties of the fluids as it is summarized in Ginzbourg and Adler (1995). In the algorithm described in Section 3.4, these coefficients

are updated in order to take into account the changes in the physical properties of the fluids.

Model 1

$$L = \begin{cases} L^{\mathrm{R}}, & \rho_{\mathrm{R}}(\mathbf{r}, t) > \rho_{\mathrm{B}}(\mathbf{r}, t), \\ L^{\mathrm{B}}, & \rho_{\mathrm{R}}(\mathbf{r}, t) < \rho_{\mathrm{B}}(\mathbf{r}, t); \end{cases}$$

$$A_{ij} = \begin{cases} A_{ij}^{\mathrm{R}}, & \rho_{\mathrm{R}}(\mathbf{r}, t) > \rho_{\mathrm{B}}(\mathbf{r}, t), \\ A_{ij}^{\mathrm{B}}, & \rho_{\mathrm{R}}(\mathbf{r}, t) < \rho_{\mathrm{B}}(\mathbf{r}, t); \end{cases} \tag{35b}$$

Model 2

$$L = \begin{cases} L^{\mathrm{R}}, & \rho_{\mathrm{B}}(\mathbf{r}, t) = 0, \\ L^{\mathrm{int}}, & \rho_{\mathrm{R}}(\mathbf{r}, t) \neq 0,\ \rho_{\mathrm{B}}(\mathbf{r}, t) \neq 0, \\ L^{\mathrm{B}}, & \rho_{\mathrm{R}}(\mathbf{r}, t) = 0; \end{cases}$$

$$A_{ij} = \begin{cases} A_{ij}^{\mathrm{R}}, & \rho_{\mathrm{B}}(\mathbf{r}, t) = 0, \\ A_{ij}^{\mathrm{int}}, & \rho_{\mathrm{R}}(\mathbf{r}, t) \neq 0,\ \rho_{\mathrm{B}}(\mathbf{r}, t) \neq 0, \\ A_{ij}^{\mathrm{B}}, & \rho_{\mathrm{R}}(\mathbf{r}, t) = 0; \end{cases} \tag{35c}$$

The condition of mass conservation imposed on the matrix $\mathbf{A}$ can be expressed by

$$\sum_{j=0}^{24} A_{ij} W_j = 0, \quad W_0 = L, \quad W_i = 1, \quad i = 1, \ldots, 24 \tag{35d}$$

Consequently, when the matrix $\mathbf{A}(\mathbf{r}, t-1)$ has to be replaced by some different matrix $\mathbf{A}(\mathbf{r}, t)$, the value of rest population $N_0'(\mathbf{r}, t)$ has to be recalculated before collision in order to conserve mass during the collision, if the numbers of rest populations associated with these matrices are different

$$N_0'(\mathbf{r}, t) = \frac{N_0(\mathbf{r}, t) L(\mathbf{r}, t-1)}{L(\mathbf{r}, t)}. \tag{35e}$$

Each kinematic viscosity ν^{K} is defined by the eigenvalue $\lambda_{\psi}^{\mathrm{K}}$ of the corresponding collision matrix

$$\nu^{\mathrm{K}} = -\frac{c^2}{D+2}\left(\frac{1}{2} + \frac{1}{\lambda_{\psi}^{\mathrm{K}}}\right) \quad \text{for } K = \mathrm{R},\ \mathrm{B} \tag{35f}$$

Step 3 (Surface tension)**.** A perturbation $\delta N_i(\mathbf{r}, t)$ of the populations creates surface tension

$$N_i''(\mathbf{r},\ t) = N_i^*(\mathbf{r},\ t) + \delta N_i(\mathbf{r},\ t) \tag{36a}$$

$$\delta N_i(\mathbf{r},\ t) = C^{\mathrm{per}}\left(\frac{(\mathbf{C}_i\cdot\mathbf{f})^2}{(\mathbf{f}\cdot\mathbf{f})^2} - \frac{1}{2}\right)$$

where C^{per} is some function of $\mathbf{f}(\mathbf{r},\ t)$; $C^{\mathrm{per}}(\mathbf{r},\ t)$ decreases when the distance from the interface increases. A standard form for $C^{\mathrm{per}}(\mathbf{r},\ t)$ has been given by Gustensen (1992)

$$C^{\mathrm{per}}(\mathbf{r},\ t) = A^{\mathrm{per}}|\mathbf{f}(\mathbf{r},\ t)| \tag{36b}$$

where A^{per} is an arbitrary constant. The local color gradient $\mathbf{f}(\mathbf{r},\ t)$ is defined by

$$\mathbf{f}(\mathbf{r},\ t) = \sum_{i=1}^{24} \mathbf{C}_i\left[\rho_{\mathrm{R}}(\mathbf{r}+\mathbf{C}_i,\ t) - \rho_{\mathrm{B}}(\mathbf{r}+\mathbf{C}_i,\ t)\right] \tag{36c}$$

Step 4 (Recoloring)**.** The total population is recolored in order to separate the populations $N_i''\mathrm{R}$ and $N_i''\mathrm{B}$ before subsequent propagation; $N_i''\mathrm{R}(\mathbf{r},\ t)$ is set equal to a value which maximises the function $\upsilon(N_i^{\mathrm{R}})$

$$\upsilon\left(N_i^{\mathrm{R}}\right) = \sum_{i=1}^{24} N_i^{\mathrm{R}}\mathbf{C}_i\cdot\mathbf{f}(\mathbf{r},\ t) \tag{37a}$$

together with the constraints

$$\sum_{i=0}^{24} N_i^{\mathrm{R}} W_i^{\mathrm{R}} = \rho_{\mathrm{R}}(\mathbf{r},\ t) \tag{37b}$$

$$0 \le N_i^{\mathrm{R}} W_i^{\mathrm{R}} \le N_i''(\mathbf{r},\ t)\ W_i(\mathbf{r},\ t) \tag{37c}$$

In order to conserve the total momentum in a site, $N_i''\mathrm{B}(\mathbf{r},\ t)$ is given by

$$N_i''\mathrm{B}\,W_i^{\mathrm{B}} = N_i''W_i - N_i''\mathrm{R}\,W_i^{\mathrm{R}} \quad i = 0,\ldots,24 \tag{37d}$$

Step 5 (Propagation)**.**

$$N_i^{\mathrm{K}}(\mathbf{r}+\mathbf{C}_i,\ t+1)W_i^{\mathrm{K}} = N_i''\mathrm{K}(\mathbf{r},\ t)W_i^{\mathrm{K}},\quad i = 0,\ldots,24 \text{ for } K = \mathrm{R},\mathrm{B} \tag{38}$$

Then the iteration procedure **1–5** is repeated.

It might be the right place to give the expression of the force $\mathbf{F}$ in Eq. (34); consider a Stokes flow in a periodic medium; it was shown in Adler (1992) that the driving force can be taken as an external macroscopic pressure drop $\overline{\nabla p}$. The velocity field $\breve{\mathbf{u}}$ is periodic and the pressure can be decomposed into a periodic $\breve{p}(\mathbf{r})$ and a linear component

$$p(\mathbf{r}) = \breve{p}(\mathbf{r}) + \mathbf{r}\cdot\overline{\nabla p}$$

When this decomposition is introduced into the Stokes equation, one obtains

$$\mu\nabla^2\breve{\mathbf{u}} = \nabla\breve{p} + \overline{\nabla p}, \quad \nabla\cdot\breve{\mathbf{u}} = 0$$

Hence, the macroscopic pressure gradient acts as an external body force. This can be easily generalized for two-phase flow, and this corresponds to the inclusion of a body force, which is equal for each phase.

3.2. Flash problem

As discussed in Section 2.4, thermodynamic equilibrium exists at the local scale.

The determination of the phase volume fractions and compositions given the pressure P, temperature T and global composition characterised by z_1 of a mixture is a task to be performed repeatedly in the simulations. It is commonly called the flash problem (Reid et al., 1987; Section 8.12). Explicitly, one has to determine the molar fractions in both phases which satisfy the equilibrium condition (17) at the liquid/vapor interface. This means solving the set of two strongly non-linear equations

$$K_1\Phi_1^{\mathrm{V}} = \Phi_1^{\mathrm{L}} \tag{39}$$

$$K_2\Phi_2^{\mathrm{V}} = \Phi_2^{\mathrm{L}}$$

where the fugacity coefficients Φ_α^β are given by Eq. (21). This can only be done by an iterative procedure. The general scheme of the method is the following:

1. Start with initial guesses for the partition coefficients K_1 and K_2. The liquid mole fraction $L = N^{\mathrm{L}}/N$ and the component mole fractions X_α^β can be deduced from Eqs. (4) and (5).
2. Determine the corresponding compressibility factors Z^{L} and Z^{V} in both phases by solving the Peng–Robinson Eq. (13a) and (13b) with Eqs. (14) and (15).
3. Calculate the fugacity coefficients Φ_α^β by Eq. (21) and deduce the new partition coefficients from Eq. (19)

$$K_\alpha = \Phi_\alpha^{\mathrm{L}}/\Phi_\alpha^{\mathrm{V}} \tag{40}$$

4. Determine new values of the mole fractions X_α^β from L and K_α, using Eq. (4)

$$X_\alpha = \frac{z_\alpha}{K_\alpha + L(1-K_\alpha)} \quad Y_\alpha = K_\alpha X_\alpha \tag{41}$$

5. Evaluate $\sum_\alpha(X_\alpha - Y_\alpha)$, which should be equal to zero when the solution is reached.
6. Adjust the liquid mole fraction L according to

$$L_{\mathrm{new}} = \mathrm{L} - \frac{\sum_\alpha\left[z_\alpha(K_\alpha-1)\right]/\left[K_\alpha + L(1-K_\alpha)\right]}{\sum_\alpha\left[z_\alpha(K_\alpha-1)^2\right]/\left[K_\alpha + L(1-K_\alpha)\right]^2} \tag{42}$$

7. Go back to step 2.

The iterative procedure stops when the error in step 5 falls below a prescribed tolerance. Values of L below 0 or above 1 denote a single phase state, vapor or liquid, respectively.

This resolution scheme is stable provided that the initial guesses for the partition coefficients in step 1 are close enough to the solution. This is easily achieved if the flash problem has previously been solved under slightly different (P, z_1) conditions, as it often happens in the study of the mixture evolution along the flow. However, such hints are not available for the very first resolution. If the mixture is single-phase, a gross estimate of K_α is sufficient. For the numerical applications in this study, a couple of values slightly apart from one (e.g. 0.9 and 1.1) were found satisfactory. In other cases, a few trials should easily yield convenient values. If the mixture consists of two phases, sharper guesses for the K_α are required. We used the following method. Suppose that the flash problem is to be solved for (P, z_1). We simulate the flow of a mixture with composition z_1 at $P_0 > P$. P_0 is set high enough so that the mixture is single-phase and rough estimates of K_α are sufficient. For the pressure P, we obtain the partition coefficients corresponding to a composition z_1', not too different from z_1, which can be used as initial guess for the actual problem.

Once the mixture composition is known, the various parameters of interest and physical coefficients can be obtained from the equations in Section 2.2

3.3. General algorithm

The calculations of the evolution of the flow through the porous medium can be made as follows. They consist of the following steps which are schematized in Fig. 3. The temperature is assumed to be uniform and equal to its initial value T throughout the reservoir; the mixture consists of only two components.

3.3.1. Reservoir and single phase region

One starts from known initial conditions in the reservoir with pressure P, global molar fraction $z_1{}^\circ$ of component 1 (or for sake of brevity composition), global mass flux Q_0. The mass flow rate of each component is also known and constant

$$q_1 = q_{10} \quad q_2 = q_{20} \tag{43}$$

It is assumed that the reservoir conditions correspond to a single phase situation; when this is not true, the algorithm is started at the beginning of loop 1. The flow of a single phase is easily determined by some single phase code and one derives the pressure gradient for the global mass flux which is known. Hence, since in single phase flow the composition does not change, one can determine the pressure P_1 for which the double phase regime starts. The corresponding abscissa x_1 is calculated with the pressure gradient. All the related physical properties are obtained for this pressure.

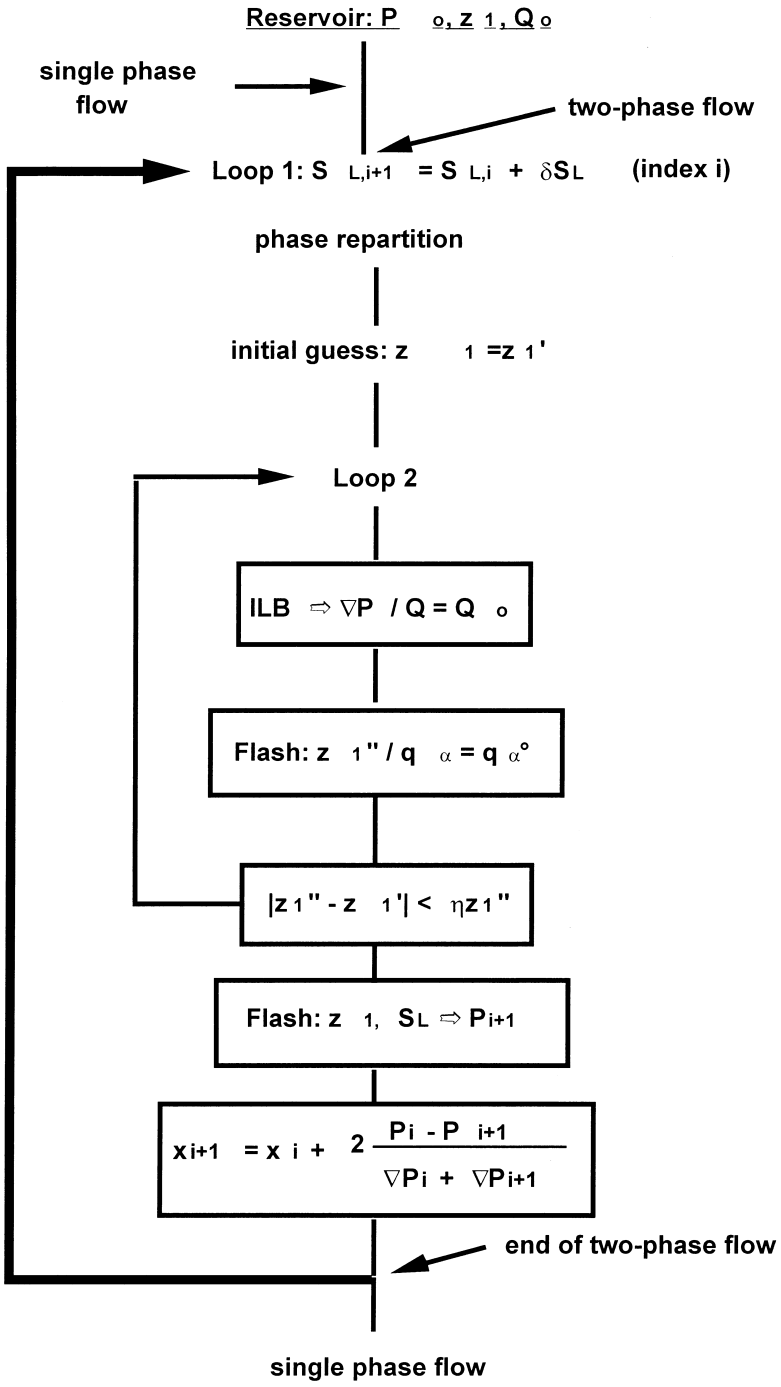

Fig. 3. General algorithm.

3.3.2. Evolution of the two-phase flow along x

3.3.2.1. Beginning of loop 1. The nature of the problem now changes completely when two-phase flow occurs. Let i be the index of loop 1 which corresponds to the saturation steps which are going to be imposed to the mixture. At the beginning of loop 1, this index is equal to 1.

Generally speaking, consider that this index has the value i. All the relevant quantities are supposed to be known; at point x_i, the pressure P_i, the composition $z_{1,\,i}$, the saturation $S_{\mathrm{L},\,i}$ and the pressure gradient ∇P_i are known. These quantities are well defined because of the assumption of local equilibrium, as imposed by Eqs. (1), (33a) and (33b) and as discussed in Section 2.4. Now assume that a variation of the saturation is imposed at the intermediate scale $\mathscr{L}$

$$S_{\mathrm{L},\,i+1} = S_{\mathrm{L},\,i} + \delta S_{\mathrm{L}} \tag{44}$$

where δS_{L} is a given variation which can be changed. One wants to determine the new values x_{i+1}, P_{i+1}, $z_{1,\,i+1}$, and ∇P_{i+1} for which this new saturation is obtained. Note that $\delta \mathrm{S}_{\mathrm{L}}$ can be either positive or negative and that its sign may change along a given path in retrograde condensation.

A phase distribution inside the pore space has also to be determined. Two different situations may exist. If it is the first time that one enters loop 1 (i.e. $i = 1$), the new phase is arbitrarily distributed; some examples of this arbitrary character will be given in Section 5.1. If $i > 1$, the new phase distribution is obtained by peeling one of the existing phases according to the sign of δS_{L}.

This peeling process can be described as follows. The layer located at the interface between the two phases is changed into the phase which is getting larger as indicated by the sign of δS_{L}; moreover, the number of modified populations correspond to the magnitude of δS_{L}.

3.3.2.2. Loop 2. In order to determine the set of values $\{x_{i+1},\ P_{i+1},\ z_{1,\,i+1},\ \nabla P_{i+1}\}$, a new iteration loop is started which is denoted as loop 2 in Fig. 3. This loop 2 is located inside loop 1. The major variable of this loop is the composition z_1. Let z_1' is a new value of z_1.

First the lattice Boltzmann code is used in order to determine the pressure gradient ∇P_{i+1} for which the overall mass flow rate is equal to its constant value Q_0. The physical properties of the two phases are calculated according to the prevailing conditions; the coefficients of the collision matrix Eqs. (35a)–(35f) are modified accordingly. The flow rates are of course time-averaged in order to be meaningful; when these averages are stabilized, a new phase distribution is obtained.

Second, the flash program is called and a new value z_1'' of z_1 is determined in such a way that for the new saturation $S_{\mathrm{L},\,i+1}$, the mass flow rates of each component are equal to the initial mass flow rates q_{1o} and q_{2o}.

Third, the two values z_1' and z_1'' are compared. If the difference is too large, loop 2 is started again with $z_1' = z_1''$ and updated physical properties. This criterion is precisely stated as

$$|z_1'' - z_1'| < \eta z_1'' \tag{45}$$

At this point loop 2 is completed; saturation and composition are known; pressure can be deduced by again using the flash program.

3.3.2.3. End of loop 1

We also know the new pressure gradient ∇P_{i+1} because of the lattice Boltzmann program. Hence, the new abscissa inside the reservoir can be determined by using the following formula

$$x_{i+1} = x_i + 2\frac{P_i - P_{i+1}}{\nabla P_i + \nabla P_{i+1}} \tag{46}$$

Hence, all the new values are determined and loop 1 can be started again with a new variation of the saturation.

These calculations can be continued until the end of the two-phase flow region.

3.4. Final single phase region

The single phase calculations are started again. Note that the composition of the single phase fluid is necessarily identical to the initial composition. The calculations can be continued until the end of the reservoir.

3.5. General conditions

In this paragraph, the general conditions under which we are working, are given in detail; they will be valid for most of the rest of this paper.

Due to the applications which motivated this study, the temperature is chosen equal to 100F or 37.8°C; since the flow rates are rather small, the temperature is assumed to be constant throughout the reservoir. The pressure P_0 in the reservoir is equal to 91 bars. Also a methane/propane mixture is always used; component $\alpha = 1$ is methane. Under these circumstances, the liquid saturation as a function of the pressure and of the global mole fraction z_1 of methane is displayed in Fig. 4.

Two initial compositions have been chosen. ${z_1}^\circ = 0.5$ yields a monotonous liquid to gas evolution, while ${z_1}^\circ = 0.6$ displays a zone where retrograde condensation occurs.

A last general feature was found useful. Instead of giving the distances in meters, it turned out to be more convenient to use a reduced distance $\hat{x}$ whose dimension is equal to pressure (Pascal)

$$\hat{x} = \frac{\mu_0}{K}\frac{Q_0}{\rho_0}x \tag{47a}$$

where K is the permeability of the porous medium. μ_0 and ρ_0 are evaluated at the reservoir conditions ($T_0 = 37.8$°C, $P_0 = 91$ bars). The origin of the x-axis is located at the reservoir.

The major physical properties are given in Table 2, together with the viscosity ratio m (cf. Eq. (10)) and the capillary number

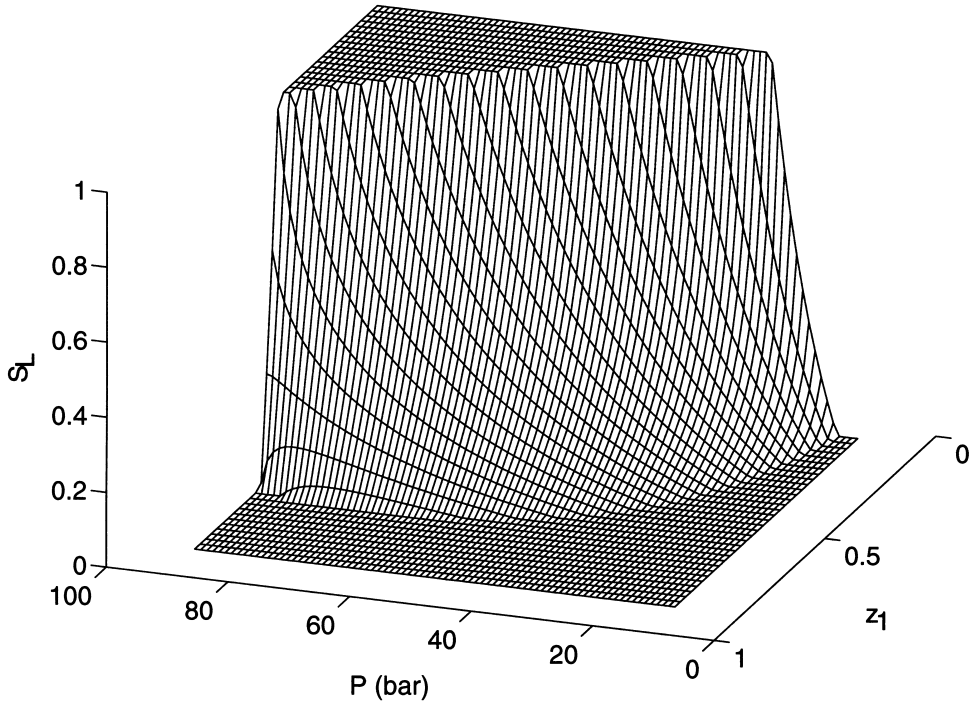

Fig. 4. The liquid saturation S_L for a methane/propane mixture at $T = 37.8°C$ (100F) as a function of pressure P and global mole fraction z_1 of methane. P varies from 13 to 90 bar in 1 bar steps, and z_1 from 0.05 to 0.9 in 0.025 steps.

Table 2
Physical properties at the reservoir conditions and at the dew point[a]

Initial global molar fraction of methane	At the reservoir conditions	At the dew point
Liquid–gas transition $z_1^\circ = 0.5$	$\mu^L = 2.1 \times 10^{-5}$, $\rho_0^L = 282.2$ kg/m^3, $T = 37.8°C$	$P = 88.3 \times 10^5$, $\mu^L = 2.113 \times 10^{-5}$, $\mu^V = 2.595 \times 10^{-5}$, $m = 1.23$, $\sigma_0 = 1.45 \times 10^{-5}$, $\rho_0^L = 227.4$ kg/m^3, $Ca = 0.52 \times 10^{-2} Q_0$
Retrograde condensation $z_1^\circ = 0.6$	$\mu^V = 1.9 \times 10^{-5}$, $\rho_0^V = 198.5$ kg/m^3, $T = 37.8°C$	$P = 90.18 \times 10^5$, $\mu^L = 1.2 \times 10^{-5}$, $\mu^V = 1.87 \times 10^{-5}$, $pm = 1.56$, $\sigma_0 = 2.61 \times 10^{-6}$, $\rho_0^V = 195.1$ kg/m^3, $Ca = 3.7 \times 10^{-2} Q_0$

[a] All the quantities are given in SI units; for instance, the global mass flux is expressed in kg/m^2 s.

$$Ca = \frac{\mu u}{\sigma} = \frac{\mu Q_0}{\sigma \rho_0} \tag{47b}$$

The velocity has been replaced by the total mass flow rate Q_0 which varies from case to case. The capillary number is given at the dew point in Table 2; it is relative to the single phase which exists in the reservoir; hence, for LV and RC, the density and the viscosity are relative to liquid and vapor, respectively.

Note that the range of values of the capillary numbers is deliberately very large; it does not really matter for the constriction and the two-dimensional network which correspond to theoretical situations. This is likely to be more important in the reconstructed medium; calculations would have been possible, but exceedingly slow.

4. Application to plane Poiseuille flow and verifications

The major purpose of this section is to make sure that the general code compares well with the results which can be derived in a semi-analytical way for the Poiseuille flow. In Section 4.1,

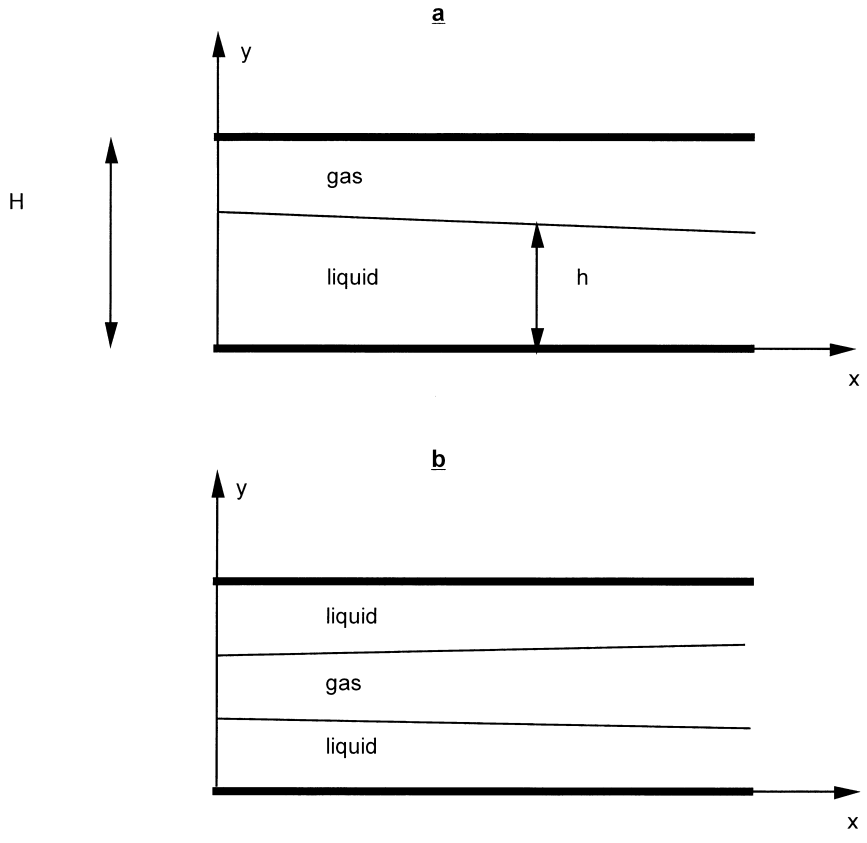

Fig. 5. Plane Poiseuille flow. (a) Asymmetric and (b) symmetric multiphase configurations.

the semi-analytical solution based on parabolic profiles will be detailed. In Section 4.2, a long series of tests will be described and the corresponding evolutions will be compared to the ones obtained with the code presented in the previous section.

4.1. Semi-analytical calculation for plane Poiseuille flow

The physical situation is depicted in Fig. 5(a). A plane channel of width H is partially filled by a height h of liquid; note that this filling is made in an asymmetric way. Define

$$\tilde{h} = \frac{h}{H} \tag{48}$$

In agreement with our general assumption of slow variations at the local scale which is discussed in Section 2.4, the flow is almost established with slow variations of h, so that the velocity profile in each phase is parabolic. They are expressed by

$$u^{\mathrm{V}} = -\frac{H^2}{2\mu^{\mathrm{V}}}\left[1-\tilde{y}\right]\left[\tilde{y}-\tilde{h}+\frac{m\tilde{h}}{m\tilde{h}+1-\tilde{h}}\right]\frac{\mathrm{d}P}{\mathrm{d}x}$$

$$u^{\mathrm{L}} = -\frac{H^2}{2\mu^{\mathrm{L}}}\tilde{y}\left[\tilde{h}-\tilde{y}+\frac{1-\tilde{h}}{m\tilde{h}+1-\tilde{h}}\right]\frac{\mathrm{d}P}{\mathrm{d}x} \tag{49}$$

Under stationary conditions, the mass fluxes q_1 and q_2 of both components have to remain constant through all the cross-sections of the channel. These two fluxes can be calculated analytically given (P, z_1) (and thus the mixture composition) by a straightforward integration of Eq. (49)

$$q_\alpha = -\frac{H^2}{12A_0^2}\left(\frac{\rho_\alpha^{\mathrm{L}}A^{\mathrm{L}}}{\mu^{\mathrm{L}}}+\frac{\rho_\alpha^{\mathrm{V}}A^{\mathrm{V}}}{\mu^{\mathrm{V}}}\right)\frac{\mathrm{d}P}{\mathrm{d}x} \tag{50a}$$

where the coefficients are given by

$$A_0 = (m-1)\tilde{h}+1$$

$$A^{\mathrm{L}} = (1-m)^2\tilde{h}^5+(1-m)\tilde{h}^4+(3m-5)\tilde{h}^3+3\tilde{h}^2$$

$$A^{\mathrm{V}} = -(1-m)^2\tilde{h}^5+\left(6m^2-11m+5\right)\tilde{h}^4-\left(9m^2-21m+10\right)\tilde{h}^3+\left(4m^2-17m+10\right)\tilde{h}^2+5(m-1)\tilde{h}+1 \tag{50b}$$

where m is the viscosity ratio Eq. (10).

These fluxes may be expressed differently by using the following relations. The thickness of the liquid layer within the channel is given by

$$h = \frac{N_\alpha^{\mathrm{L}} M_\alpha}{\rho_\alpha^{\mathrm{L}}} = \frac{N^{\mathrm{L}} M^{\mathrm{L}}}{\rho^{\mathrm{L}}}$$

where M^β is an equivalent molar mass

$$M^\beta = X_1^\beta M_1 + X_2^\beta M_2$$

Finally, note that the densities ρ_α^{L} in the liquid and ρ_α^{V} in the vapor are related by

$$\rho_\alpha^{\mathrm{L}} = \frac{1}{K_\alpha}(1-\tilde{h})\frac{N^{\mathrm{L}}}{N^{\mathrm{V}}}\rho_\alpha^{\mathrm{V}}$$

Introduction of these relations into the previous expression yields

$$q_\alpha = -\frac{H^2}{12A_0^2}\frac{\rho_\alpha^{\mathrm{V}}}{\mu^{\mathrm{V}}}\left(\frac{m}{K_\alpha}\frac{1-\tilde{h}}{\tilde{h}}\frac{N^{\mathrm{L}}}{N^{\mathrm{V}}}A^{\mathrm{L}} + A^{\mathrm{V}}\right)\frac{\mathrm{d}P}{\mathrm{d}x} \tag{51a}$$

Equivalently, the partial mass fluxes $\overline{q_\alpha}$ are written as (cf. Eq. (11))

$$\overline{q_\alpha} = \frac{q_\alpha}{q_1+q_2} = \frac{\rho_\alpha^{\mathrm{V}}\left(\frac{m}{K_\alpha}\frac{1-\tilde{h}}{\tilde{h}}\frac{N^{\mathrm{L}}}{N^{\mathrm{V}}}\frac{A^{\mathrm{L}}}{A^{\mathrm{V}}}+1\right)}{\sum_\alpha \rho_\alpha^{\mathrm{V}}\left(\frac{m}{K_\alpha}\frac{1-\tilde{h}}{\tilde{h}}\frac{N^{\mathrm{L}}}{N^{\mathrm{V}}}\frac{A^{\mathrm{L}}}{A^{\mathrm{V}}}+1\right)} \tag{51b}$$

First note that Eq. (51b) can be summarized by the simple statement that $\overline{q_1}$ is constant along the channel. Observe that $\overline{q_1}$ can be evaluated at any point where P and z_1 are known. Indeed, the right-hand-side of Eq. (51b) only contains quantities which can be deduced from P and z_1. It is remarkable that the partial mass fluxes $\overline{q_\alpha}$ depend only on the reservoir conditions (P, z_1), irrespective of the channel height H or global mass flux Q. Of course, this property holds only for the simple geometry under consideration, although similar results can be expected in other configurations, as long as surface tension effects can be ignored.

Knowing $\overline{q_1}$, it is a simple task to determine z_1 for any given pressure, by solving Eq. (51b), which is an equation of the general form

$$F(P, z_1) = q_1 \tag{52}$$

Eq. (52) is strongly non-linear. In the program, an alternative form of Eq. (51b) is solved, namely

$$m\frac{1-\tilde{h}}{\tilde{h}}\frac{N^{\mathrm{L}}}{N^{\mathrm{V}}}\frac{A^{\mathrm{L}}}{A^{\mathrm{V}}} = K_1K_2\frac{\frac{q_1}{M_1Y_1}-\frac{q_2}{M_2Y_2}}{\frac{q_2}{M_2X_2}-\frac{q_1}{M_1X_1}} \tag{53}$$

An iterative procedure, based on a standard Newton's method, is used for this purpose.

As a consequence of Eq. (52), the possible evolutions of the mixture starting from given conditions can be drawn as a series of paths in the (P, z_1)-space, irrespective of the actual flow conditions. Examples are presented in Fig. 6(b), relative to the standard methane/propane mixture at $T = 37.8°\mathrm{C}$. If the mole fraction $z_{1(91)}$ at $P = 91$ bars is larger than 0.65,

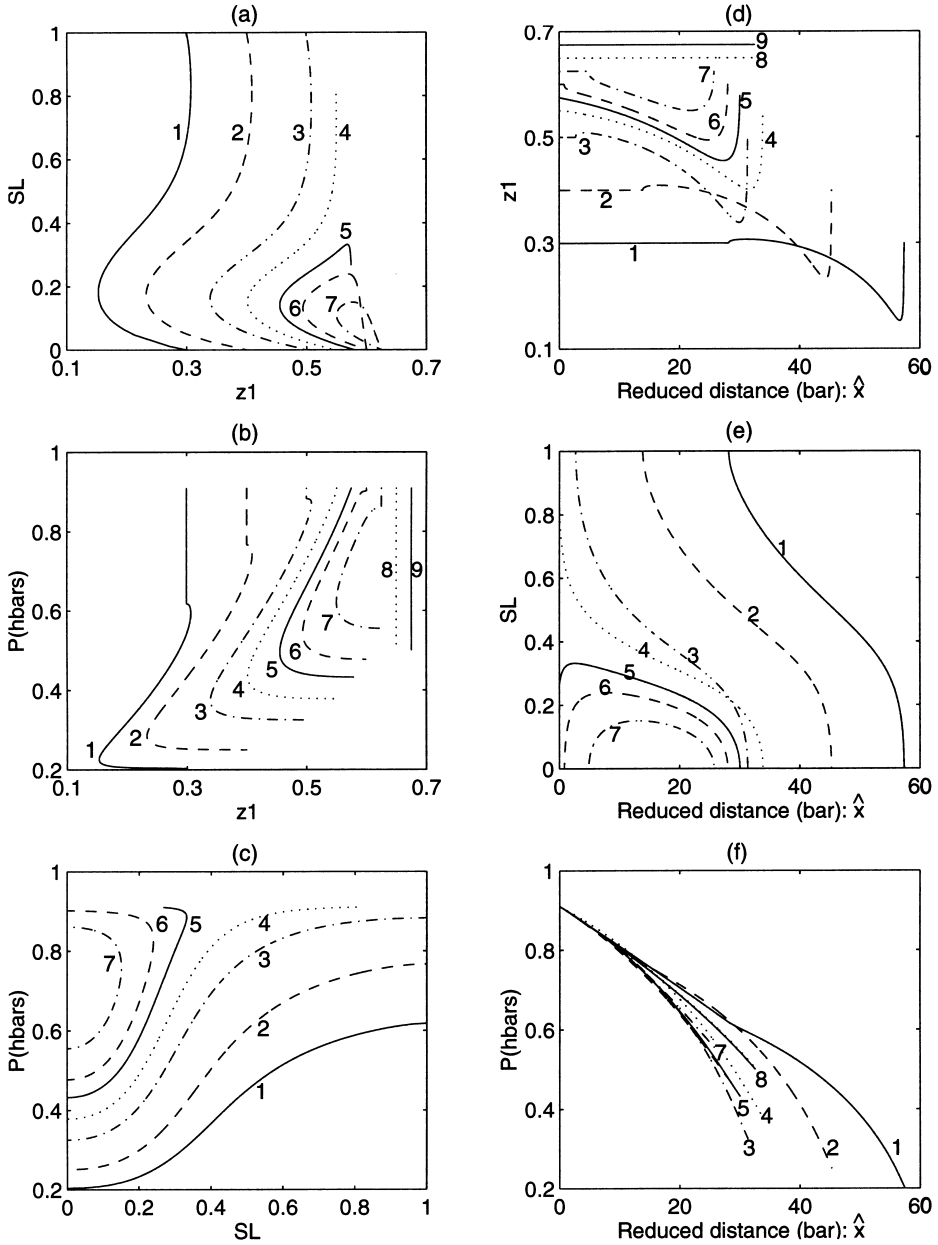

Fig. 6. The asymmetrical phase distribution for a plane Poiseuille flow. The left column corresponds to the plot of the macroscopic physical quantities as functions of one another. The right column corresponds to the plot of these quantities as functions of the reduced distance $\hat{x}$. (a) Data are for the following initial values of z_1: 1 (0.3), 2 (0.4), 3 (0.5), 4 (0.55), 5 (0.575), 6 (0.6), 7 (0.625). In (b) other values have been added which correspond to single phase evolutions: 8 (0.65), 9 (0.675).

the mixture remains monophasic for all P. Consequently, z_1 does not vary. At lower concentrations of methane, phase changes occur and induce composition variations. When $z_{1(91)}$ decreases, the transition to pure vapor at low pressure causes a very sharp return to the initial composition.

We now turn to the simulation of an actual flow through the channel. As shown in the previous paragraph, the mixture evolution in the (P, z_1)-space is determined by the upstream conditions only. However, to make the connection between the evoluting thermodynamical state and the position along the x-axis, the channel height H and the global mass flux Q_0 have to be specified. Define a reference viscosity μ_0, and the dimensionless quantities

$$\tilde{\rho}^{\mathrm{V}} = \rho^{\mathrm{V}}/\rho_0$$

$$\tilde{\mu}^{\mathrm{V}} = \mu^{\mathrm{V}}/\mu_0 \tag{54a}$$

Then, use the definition Eq. (47a) of the reduced distance $\hat{x}$ and sum the dynamic equation Eq. (51b) over components 1 and 2; we obtain

$$\frac{\mathrm{d}P}{d\hat{x}} = -\left(\frac{A_0^2}{A^{\mathrm{V}}}\frac{\tilde{\mu}^{\mathrm{V}}}{\tilde{\rho}^{\mathrm{V}}}\frac{1}{1+m\frac{1-\tilde{h}}{\tilde{h}}\frac{N^{\mathrm{L}}}{N^{\mathrm{V}}}\frac{A^{\mathrm{L}}}{A^{\mathrm{V}}}\frac{M^{\mathrm{L}}}{M^{\mathrm{V}}}}\right) \tag{54b}$$

This is a classical relationship between the pressure gradient and the flow rate in a layered plane Poiseuille flow. If the flow is single-phase (β), Eq. (54b) reduces to

$$\frac{\mathrm{d}P}{\mathrm{d}x} = -\frac{12\mu^{\beta}}{H^2\rho^{\beta}}Q_0$$

or equivalently, with the introduction of permeability

$$\frac{\mathrm{d}P}{\mathrm{d}\hat{x}} = -\frac{12}{H^2}K \tag{54c}$$

Hence, a remarkable result of these transformations and of the use of the reduced distance is that all the quantities in the right-hand-side of Eqs. (54a)–(54c) depend only on the local pressure P.

The numerical simulations are conducted by varying P by constant steps δP, in order to cope more easily with possible sharp variations of the state variables. This detailed procedure is thus different from the general algorithm where saturation steps were imposed. If such singularities arise, for example at a transition from a single-phase to a two-phase flow, constant pressure steps ensure that the phenomena are accurately represented. In some sense, it corresponds to a spatial mesh refinement in the transition regions. The iterative procedure may be schematized by

1. Given the initial conditions (P, z_1), evaluate $\overline{q_1}$, the various mole fractions and the physical constants at $x = 0$.
2. Vary P by δP. The corresponding abscissa δx is determined by inverting Eqs. (54a)–(54c).

Simultaneously, determine the new composition z_1 by solving Eq. (52), and calculate the corresponding mole fractions, volume fractions and physical constants by solving the flash problem.

3. Repeat step 2.

It should be noted that since the thermodynamical variables for a given pressure are always evaluated only as functions of P and the partial mass flux $\overline{q_1}$ determined once for all at $x = 0$, there is no risk to accumulate errors in this respect. The only possible cumulative error concerns the relation $P(\mathbf{x})$. The relevant parameter here is the pressure step δP.

Systematic results are displayed in Fig. 6. All these results are independent of the flow rates. The reference viscosity μ_o is always taken at $P = 91$ bars for the phase present at the reservoir conditions (cf. Table 2). In addition, if $K = 0.2 \times 10^{-12}$ m^2, the distance is related to the reduced distance by

$$x = 0.208\frac{\hat{x}}{Q_0} \quad \text{for } z_{1(91)} = 0.6$$

$$x = 0.268\frac{\hat{x}}{Q_0} \quad \text{for } z_{1(91)} = 0.5 \tag{55}$$

Except for Fig. 6(b), where it is shown that flow remains single phase for $z_1{}^\circ > 0.65$, a series of initial compositions have been chosen which vary between 0.3 and 0.625. Various representations can be chosen to display the evolution of the three major variables; may be the easiest ones to consider is when they are given as functions of the reduced distance $\hat{x}$. This is shown in Fig. 6(d)–(f). As expected the evolution of the liquid saturation in Fig. 6(e) provides two regimes depending upon the initial composition. When $z_1{}^\circ$ is smaller than approximately 0.56, the fluid undergoes a liquid to gas transformation; but when $z_1{}^\circ$ is larger than this value, but smaller than 0.63 (see Fig. 4), the gas condensates partially and then vaporizes entirely again. This is also seen differently in Fig. 6(a), where the loops correspond to retrograde condensation; in this representation, S_L and z_1 go back to their initial values.

The second interesting item is the evolution of the pressure and composition along x. The evolution of the pressure is significantly influenced by the value of the initial composition; when $z_1{}^\circ = 0.3$, the reduced distance for a given pressure drop is the largest one; the distance is then significantly reduced by a factor 0.6 for $z_1{}^\circ = 0.5$.

The composition z_1 always displays the same behaviour whatever its initial value is when the second phase appears, the composition starts decreasing until some minimal value and then increases to its initial value that it reaches when a single phase remains. However, we shall see at the end of this Section that this is not a general feature; it is caused by the fact that the second phase in its initial growth remains close to the wall, in a low velocity region.

More complex representations can be used when one variable is plotted as a function of one of the two others; this is done in Fig. 6 (a)–(c). The most impressive feature of these representations is the loop that the saturation describes when it is plotted as a function of z_1

when retrograde condensation occurs. These abstract representations were found useful to check the precision of our computations, since it turned out that a major cause of error in the evolution curves is Eq. (46); since it is only used to compute $\hat{x}$, the imprecision in this variable is not shown in Fig. 6(a)–(c).

Needless to say, various tests were performed in order to check the accuracy of these codes; for instance, the influence of the pressure step has been carefully studied.

4.2. Comparisons with the general code and accuracy checks

A long series of tests was actually performed which will be briefly accounted for. Three programs were used in order to predict the evolution of the fluid

The semi-analytical routine based on the parabolic profile and presented in the previous section; it will be called the analytical program for sake of brevity.

The general program described in Sections 2 and 3, but where the determination of the flow field by the lattice Boltzmann algorithm has been replaced by the parabolic profiles Eq. (49). It will be called the numerical program.

The full general program described in Sections 2 and 3, with the ILB algorithm. It will be called the ILB program.

In the numerical and the ILB programs, the evolution of the mixture is controled by two numerical parameters, namely the saturation step δS_L used in Eq. (44) and the precision parameter η used for the composition in Eq. (45).

The influence of the saturation step is shown in Fig. 7 for the two cases of a liquid to gas saturation and retrograde condensation. In these checks, an asymmetrical configuration has been used as displayed in Fig. 5(a). Two sets of data corresponding to (i) and (ii) are displayed in this figure. It is seen that the difference between these two cases is very small and is mostly due to the error made in Eq. (46); this can be proved by displaying the results as in Fig. 6(a)–(c).

The influence of η was also checked. In one case, a large value of $\eta = 0.1$ has been imposed; in the second case, a much smaller value of $\eta = 0.001$ has been used, but because of the dramatic increase of the computation time, the iterations in loop 2 were limited to 5. Again the results are very close to one-another and to the semi-analytical calculations in case (i) where the parameter η does not appear.

The full calculations performed with the lattice Boltzmann code were also compared with cases (i) and (ii). Again the agreement between the various cases is very good and the major difference can be attributed to the error made in the evaluation of the pressure gradient by the centered difference Eq. (46).

Finally, a last series of computations were done in a plane Poiseuille flow for retrograde condensation, but instead of putting the gas phase at the wall (cf. Fig. 5(a)), it is located in the central part of the channel (cf. Fig. 5(b)). Computations were made by the ILB code. Results are displayed in Fig. 8. It is interesting to note that z_1 is almost constant throughout. Comparison with the right column of Fig. 7 is also instructive, since a difference in the initial phase distribution yields important differences in the subsequent evolution of the saturation; such a behaviour will be confirmed in other geometries.

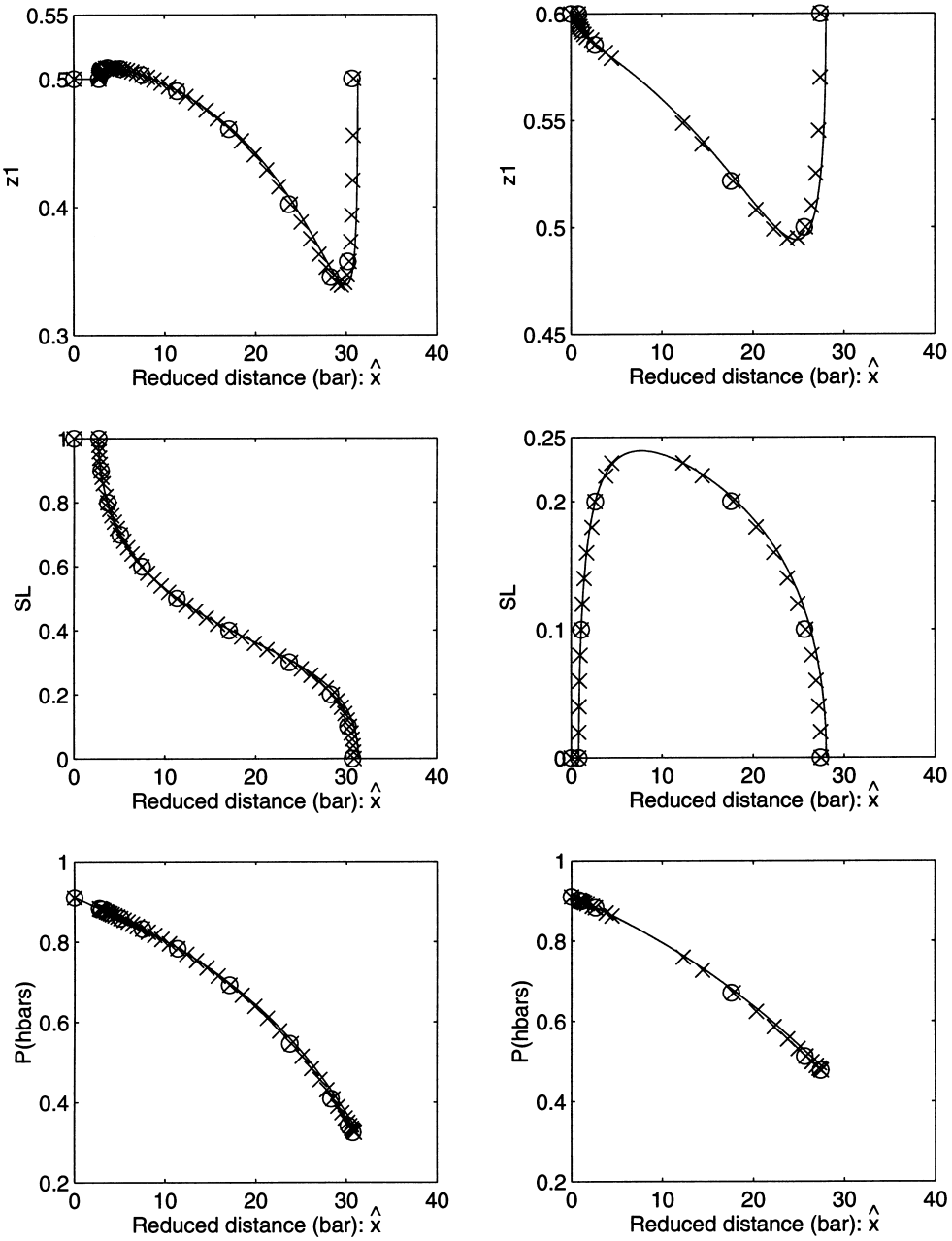

Fig. 7. Influence of the saturation step δS_L and comparison between various techniques for the asymmetrical phase distribution for a plane Poiseuille flow. The left column corresponds to a liquid to gas (LG) evolution, the right column to retrograde condensation (RC). General conditions are given in Table 2. The solid line corresponds to the analytical program. The various dots are obtained with the numerical program; saturation steps are: ○ (0.01), × (0.05).

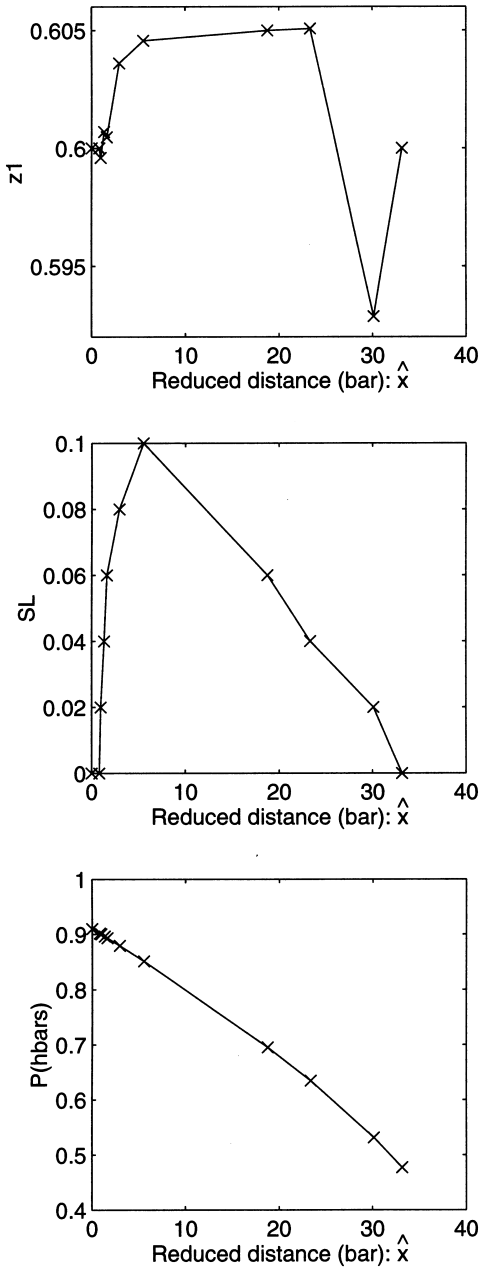

Fig. 8. Retrograde condensation for a symmetrical phase distribution in a plane Poiseuille flow. The initial composition $z_1^\circ = 0.6$. The various quantities are plotted as functions of the reduced distance $\hat{x}$.

5. Numerical applications

A series of numerical applications are given in this Section of the general algorithm described above. The two-dimensional cases have been selected because they offer the opportunity of an easy visualization of the evolution of the phases, while the three-dimensional reconstructed porous medium is closer to physical reality, but hard to visualize; in each case a particular feature will be briefly studied. Orders of magnitude of the CPU times will be given for the last two cases.

The general conditions are given in Section 3.4. Table 2 gives the physical values of the parameters. Table 3 provides all the sets of geometrical parameters which were studied, the normalized permeability K/a^2 of each configuration as well as the capillary numbers which are related to the mass flow rates which were used; the dimensional permeability of the reconstructed medium is given to be 1.85 mDarcy.

5.1. Periodic constrictions

The major purpose of this particular study is to provide an application of the ILB code in a simple case where already the velocity field is out of reach of analytical techniques. The two-dimensional porous medium is made of a periodic series of constrictions as shown in Fig. 9(a); these elementary constrictions are two-dimensional and their geometrical parameters are given in Table 2 for the sake of completeness. The channel can be decomposed into unit cells of length L as shown in Fig. 9(a); spatially periodic boundary conditions are applied and only the content of such a unit cell is displayed in Figs. 9(b) and 10.

In order to speed up the computations, the flow rates and the capillary numbers are very high; hence, they are not intended to illustrate what is usually going on in a porous medium.

In a first step, two initial compositions have been analyzed with a small and a large total mass flow rate; the second phase was assumed to appear in a symmetrical way. Then, the influence of this symmetry on the results has been studied for a large flow rate and will be shown to have a significant influence on the results.

Let us consider the liquid to gas evolution which is displayed in Fig. 10. Only the configurations where two phases are present, are displayed in this Figure. One starts from a symmetrical situation where the gas phase is assumed to fill a small plane channel in

Table 3
Geometrical parameters and capillary numbers[a]

Geometry	Geometrical parameters	Permeability K/a^2	Capillary $z_1{}^\circ = 0.5$	numbers $z_1{}^\circ = 0.6$
Constriction	$e = 5a$, $h = 30a$, $H = 90a$, $L = 25a$	31.56	10^{-4}, 13	7.4×10^{-4}, 95
Two-dimensional network	$\varepsilon = 0.64$	2.08	0.13, 13	1, 95
Reconstructed medium	$\varepsilon = 0.157$	0.445×10^{-3}	3.6×10^{-3}, 7.6×10^{-2}	2.6×10^{-2}, 2.6×10^{-1}

[a] The first line corresponds to small mass flow rates and the second line to large rates.

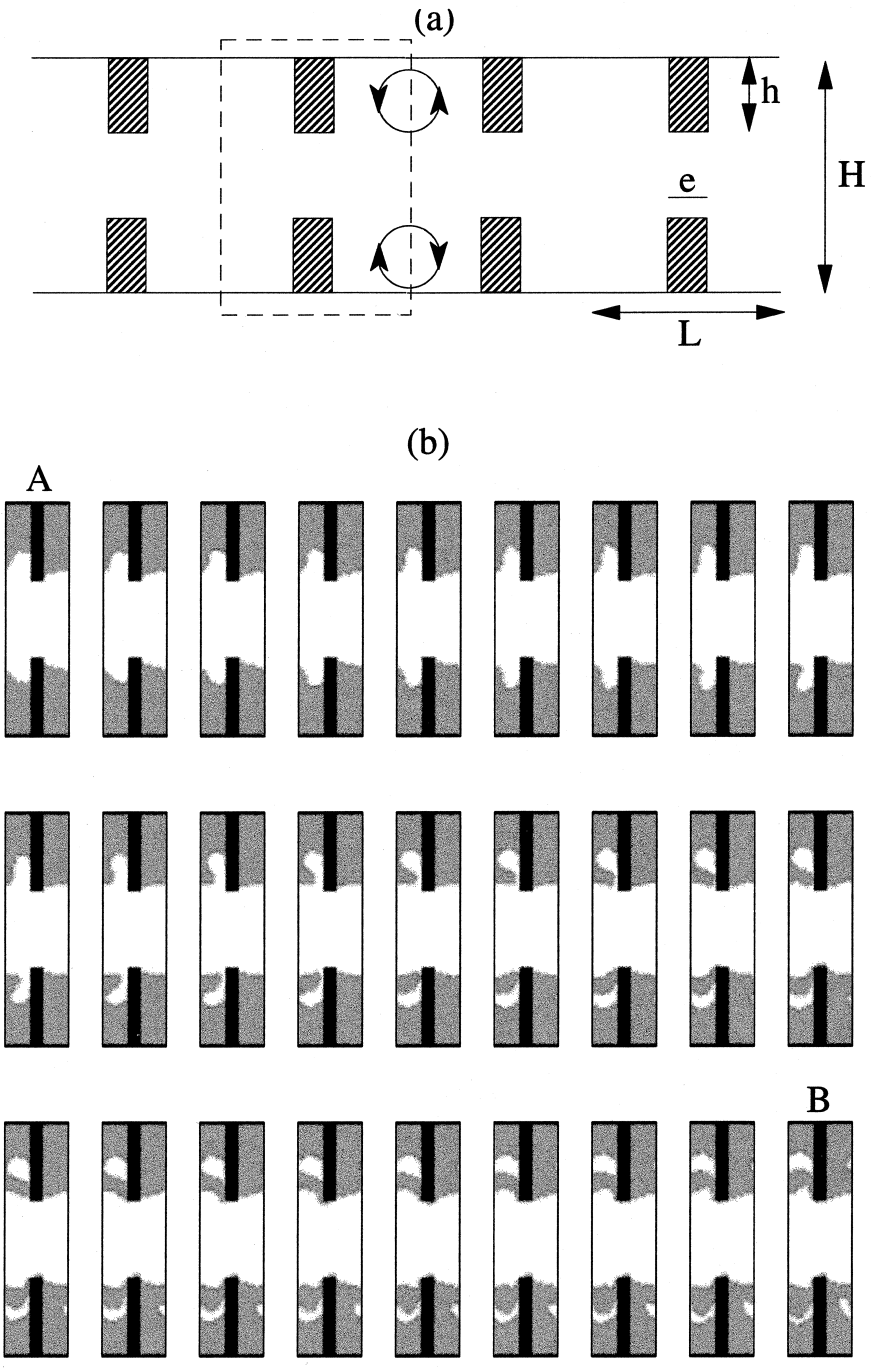

Fig. 9. Two-dimensional constriction. (a) Schematic diagram with definition of the major geometrical parameters. The unit cell is indicated by the broken lines. The streamlines are tentatively indicated by the circular solid lines with arrows. (b) Evolution of the phase distribution between stages A and B of Fig. 10; this corresponds to the application of the ILB program in loop 2 (cf. Fig. 3).

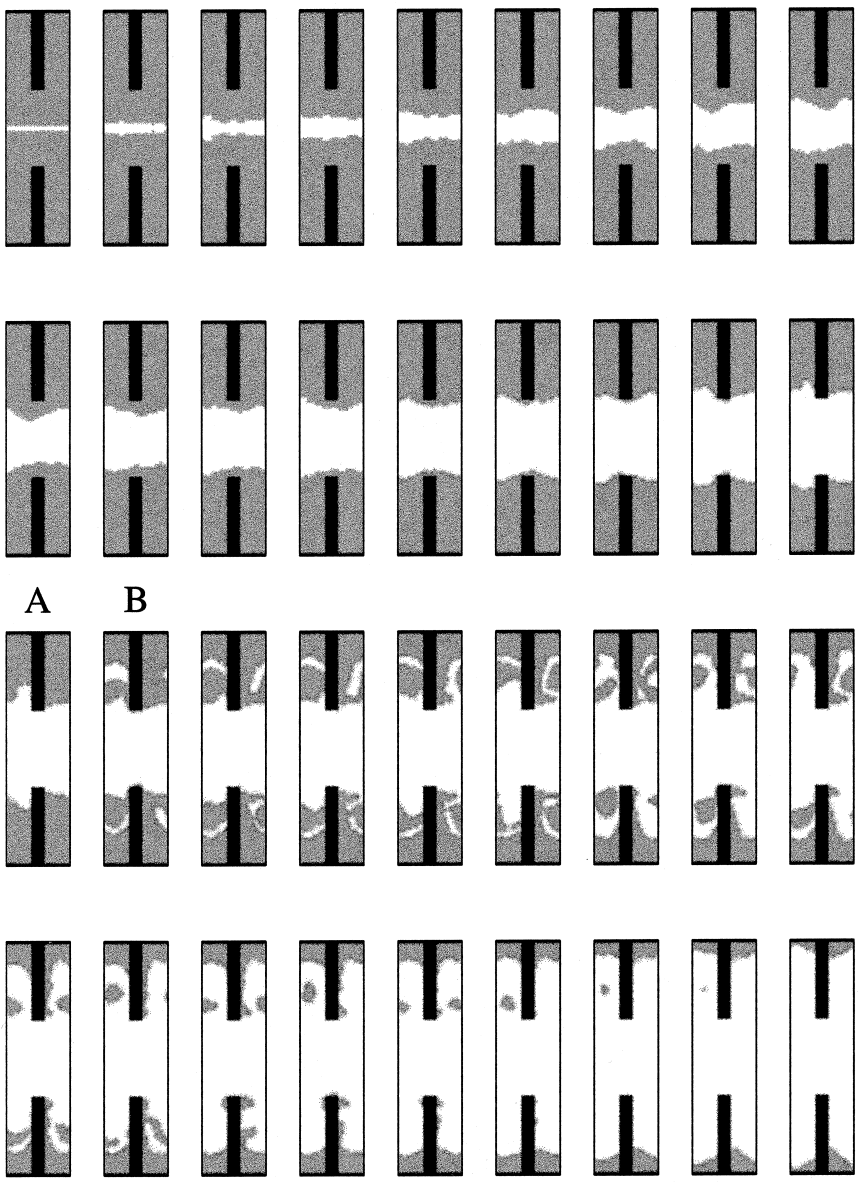

Fig. 10. Phase distribution in the two-dimensional constriction before the application of the ILB program. Data are for: initial composition $z_1{}^\circ = 0.5$; $Q_0 = 2567$ kg/m^2 s.

the middle of the constriction. Each of the subfigures of Fig. 10 corresponds to the phase distribution after the peeling stage, i.e. just before the ILB code is applied; in other words, this is at the beginning of loop 1 where a new phase distribution is proposed (cf. Fig. 3). The liquid phase disappears progressively as pressure decreases and the phase distribution retains an approximately symmetrical shape; the approximate character is due

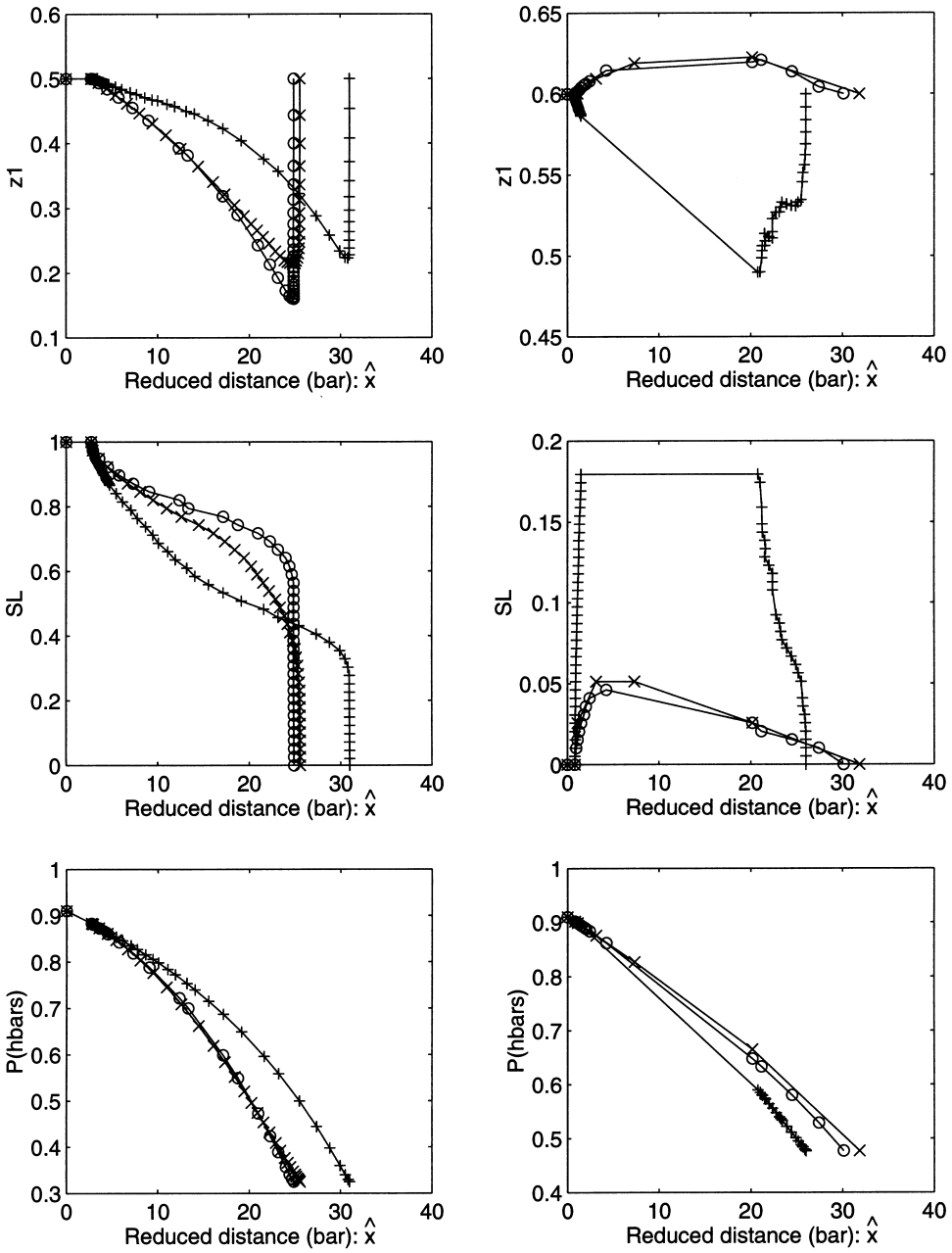

Fig. 11. Evolution of the macroscopic parameters for the two-dimensional constriction. The left column corresponds to a liquid to gas (LG) evolution, the right column to retrograde condensation (RC). General conditions are given in Table 2. Data are for: $Q_0 = 2567$ kg/m^2 s (○: symmetrical configuration; +: asymmetrical configuration), $Q_0 = 25.67$ kg/m^2 s (×: symmetrical configuration).

to the fact that the ILB code necessarily contains some fluctuations which induces, after some time, some asymmetry.

A feature is worth mentioning, namely the creation of bubbles within the dead fluid region located between the teeth of the constriction. In order to explain this feature, the evolution of the phase distribution during loop 2 when the average flow rates are determined by using the ILB code, is given in detail in Fig. 9(b) between the two steps marked by A and B in Fig. 10. Fig. 9(b) corresponds to an evolution at constant saturation; the formation of bubbles can be understood by considering the approximate picture of Fig. 9(a) which gives the streamlines in single phase between the teeth; most likely recirculation inside the dead fluid region induces an eddy which drags the central gas phase upstream as displayed in the middle line of Fig. 9(b). Then the gas phase is separated from the central stream and a bubble is formed. If one goes back to Fig. 10, one can see that after B the phase distribution tends to be more and more complex for about seven steps; however, because of the successive peelings, the distribution is progressively simplified.

The corresponding macroscopic quantities are shown in Fig. 11. There is no essential qualitative difference between this picture and the corresponding picture for Poiseuille flow in Fig. 7. The composition is drastically modified, but goes back to its initial value when liquid has disappeared totally; however, the composition variations are larger for the constriction than for the Poiseuille flow.

Similar calculations were performed for retrograde condensation. The evolution of the phase distribution is displayed in Figs. 12 and 13. In both cases, the liquid is assumed to appear first under the form of a small droplet. In Fig. 12, the droplet is located in the center of the channel; as before the symmetric configuration remains approximately symmetric along the computations; the droplet grows and the liquid saturation goes up to 0.05 and decreases back to zero. The situation is drastically changed if the initial droplet is placed in an asymmetric position as in Fig. 13; it is seen in Fig. 11 that the liquid saturation goes up to 0.18 which is more than three times the previous value; simultaneously, the composition z_1 instead of increasing starts decreasing. However, the piezometric curves do not show such drastic differences. As for the plane Poiseuille flow studied in the previous Section, the composition and the saturation differences are induced by the mass conservation of each component; when the droplet is located in the slow fluid region instead of being in the fast one, the fulfilment of these conditions induces large differences.

In a real experiment, nucleation of droplets (and of bubbles) is known to occur preferentially on heterogeneous sites which may be either at the walls or located on small impurities which are convected by the fluid; wetting properties of the solid phase also play an important role. Unless caused by specific reasons, nucleation on particles is likely to occur at random within the gas and the two situations depicted in Figs. 12 and 13 have equal probabilities; moreover, nucleation can occur at the walls. A general calculation could be done according to the following lines; the initial droplet would be located at random within the fluid phase and on the walls; the evolution curves would be the statistical averages of all the curves.

5.2. Two-dimensional network

An arbitrary two-dimensional network was used to show another application of our code to

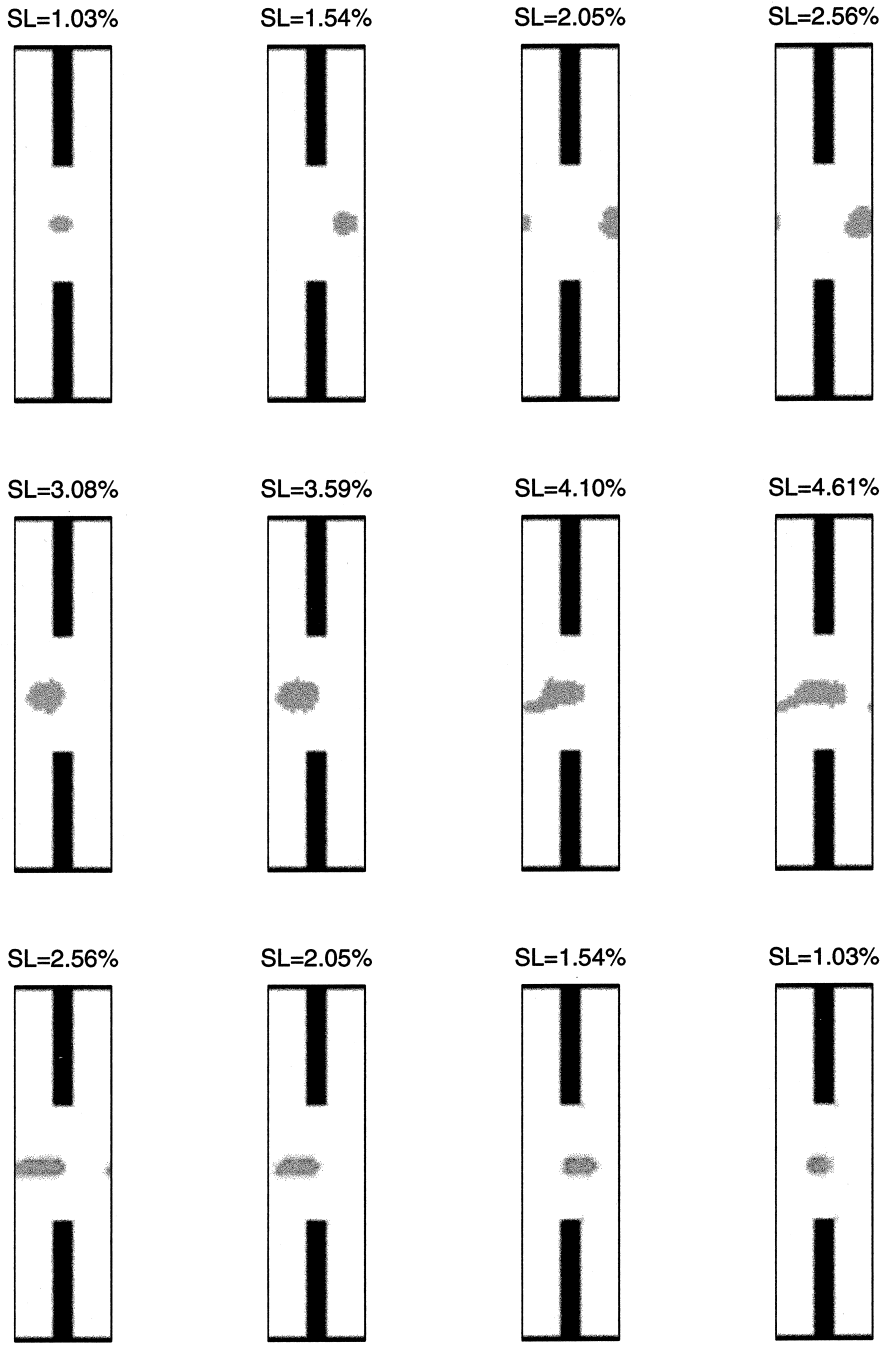

Fig. 12. Symmetrical phase distribution in the two-dimensional constriction before the application of the ILB program. Data are for: initial composition $z_1{}^\circ = 0.6$; $Q_0 = 2567$ kg/m^2 s.

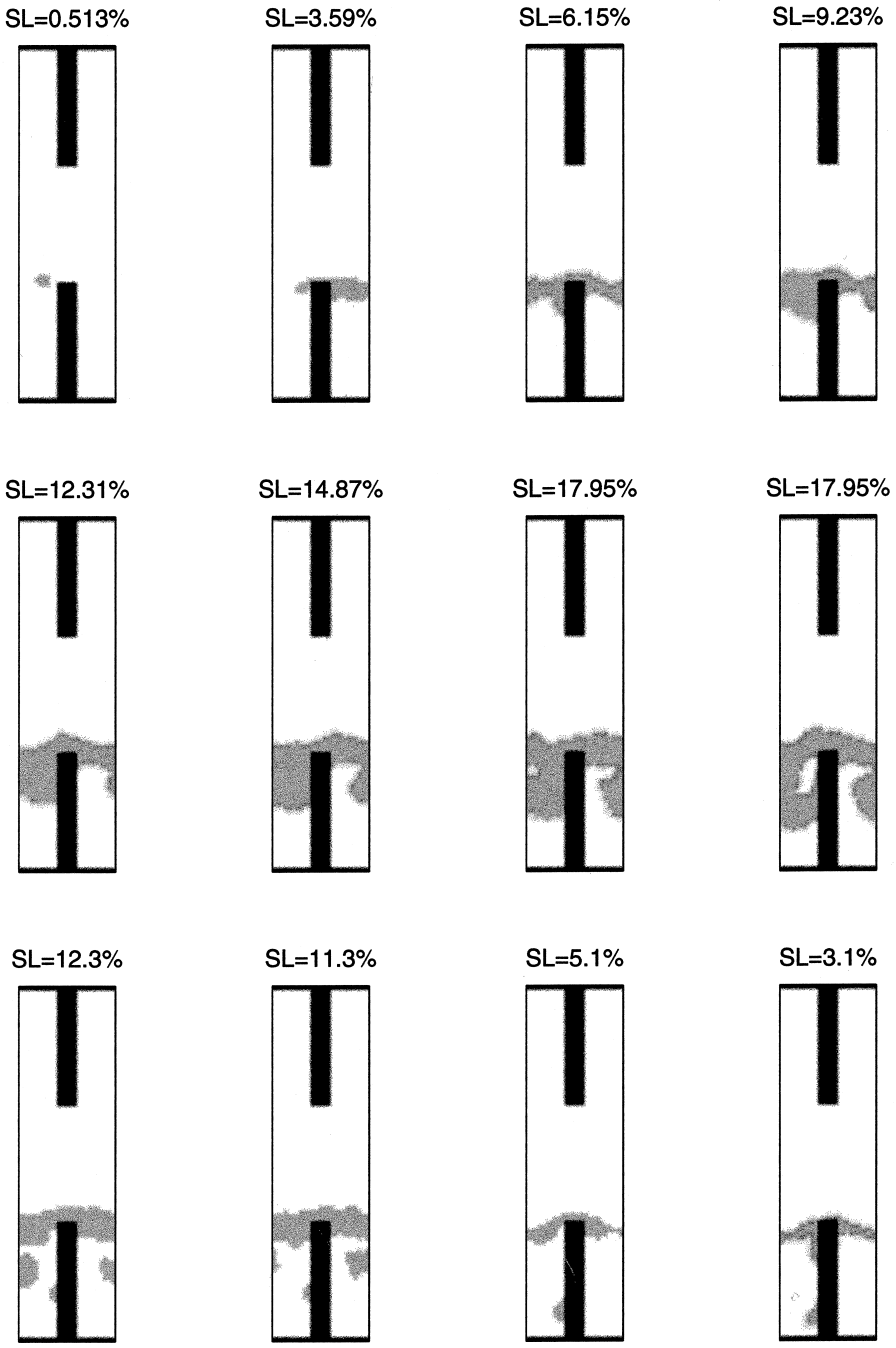

Fig. 13. Asymmetrical phase distribution in the two-dimensional constriction before the application of the ILB program. Data are for: initial composition $z_1{}^\circ = 0.6$; $Q_0 = 2567$ kg/m^2 s.

a relatively simple structure. As before four overall conditions were studied with two different compositions and two different flow rates as displayed in Table 2. On an IBM Risk station, it takes about 24 h to complete one step in the loop over saturation in Fig. 3.

One of the major aspects of this example is to clearly demonstrate the crucial importance of the flow rates on the evolution of the mixture. We always started from the same overall conditions and from the same initial phase distribution which is now perpendicular to the average pressure gradient; this configuration will hopefully ensure a good mixing of the phases within the network. For the sake of completeness, other initial phase distributions should be studied; we shall come back later on this point. In this respect, note that this network has been designed in such a way that it does not possess any symmetry; because of this feature, one may think that whatever the initial configuration, the phases will be well mixed in contrast with Poiseuille flow or the constriction where the configuration tends to keep its initial symmetry. The same remark as for the Poiseuille flow applies here since the flow rates (and the capillary numbers) are too high to be representative of standard situations in real porous media.

Let us start with a large flow rate and an initial composition $z_1 = 0.5$ which yields a liquid to gas evolution. The evolution of the phase distribution is represented in Fig. 14. The initial transversal distribution is immediately broken up into a series of small bubbles and most of them flow along the longitudinal channels. The liquid saturation decreases and when it is equal to 0.5, there is a sudden breakthrough of the gas phase through the network; subsequently, the liquid phase is mostly located in the transversal channels without a significant flow rate and it gradually disappears.

When the flow rate is divided by a factor 100, the evolution is displayed in Fig. 15. The beginning is close to the previous one with a breakup of the initial transversal gas phase into many small bubbles. However, when S_L is equal to 0.5, the two phase distributions are significantly different; now the gas phase does not make any breakthrough through the network as before, but it looks like a series of liquid and gas transversal slices; a continuous and transversal liquid phase still exists until S_L is smaller than 0.2.

The corresponding macroscopic curves are shown in Fig. 16. Again the composition and saturation curves display significant differences along the evolution while the dimensionless pressure does not change that much; this may be misleading, because of the definition, Eqs. (47a) and (47b), of the reduced abscissa; for the same real abscissa, the reduced abscissae differ by a factor 100; hence, the pressure drop for the low flow rate is comparatively much larger than that for the large flow rate.

The same computations were performed for the larger methane global molar fraction $z_1 = 0.6$ which yields retrograde condensation (see Figs. 17 and 18). For the large flow rate, the gas phase is seen to keep a continuous track across the network though the liquid saturation goes up to 0.6 (cf. Fig. 17); as before the liquid phase is mostly confined within the transversal channels with probably a low overall flow rate. The liquid saturation goes down again. Fig. 18 which corresponds to a low flow rate, displays completely different pictures since S_L only increases up to 0.16 which is about four times less than before; it seems that the liquid phase is relatively more present in the longitudinal channels than in Fig. 17 for comparable values of the liquid saturation.

The overall quantities are also displayed in Fig. 16. As previously mentioned, the maximal liquid saturations are very different, in contrast with the evolution of pressure. The

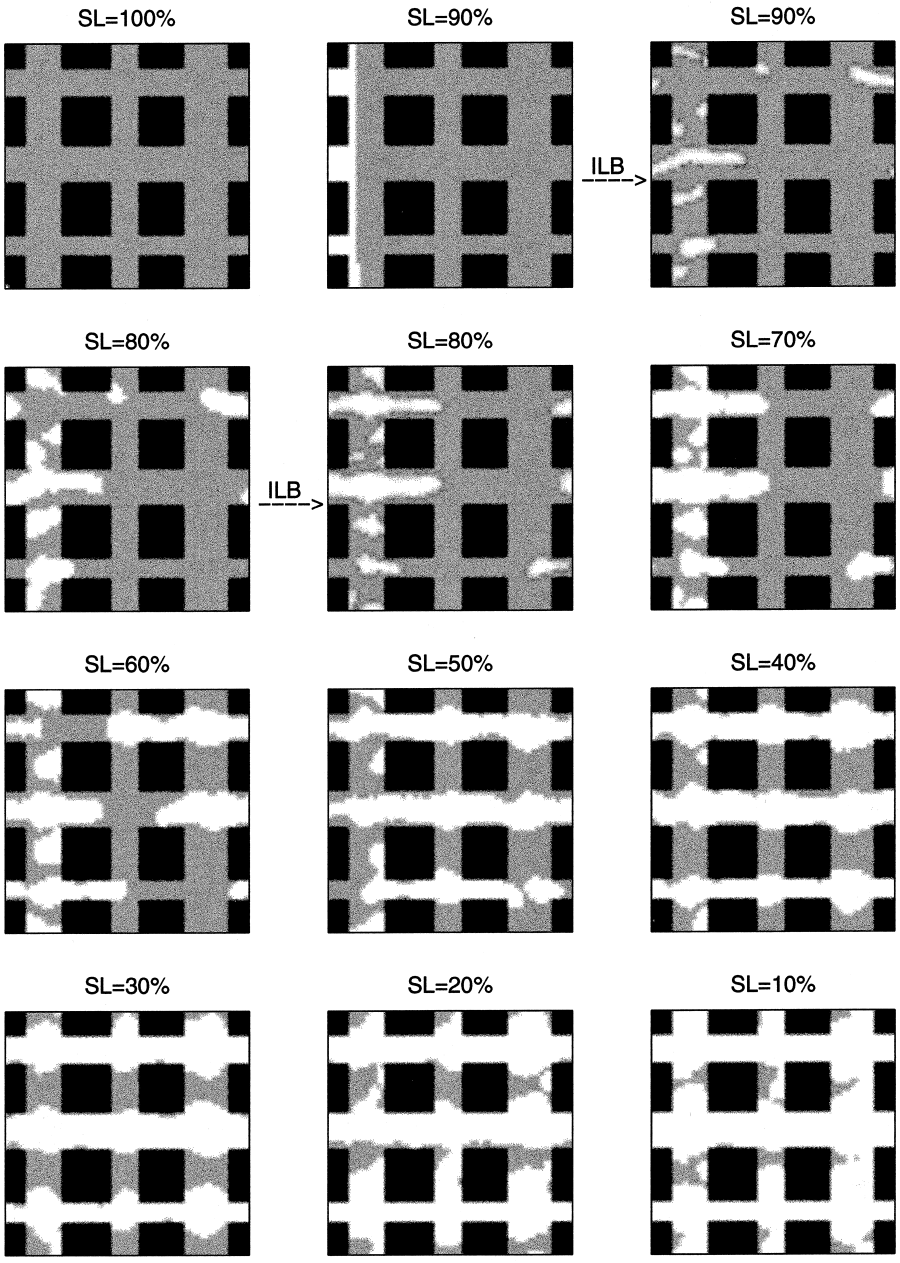

Fig. 14. Phase distribution in the two-dimensional network before the application of the ILB program, i.e. at the beginning of loop 1 where a new phase distribution is proposed (cf. Fig. 3). Data are for: LG, initial composition $z_1{}^\circ = 0.5$; $Q_0 = 2567$ kg/m^2 s.

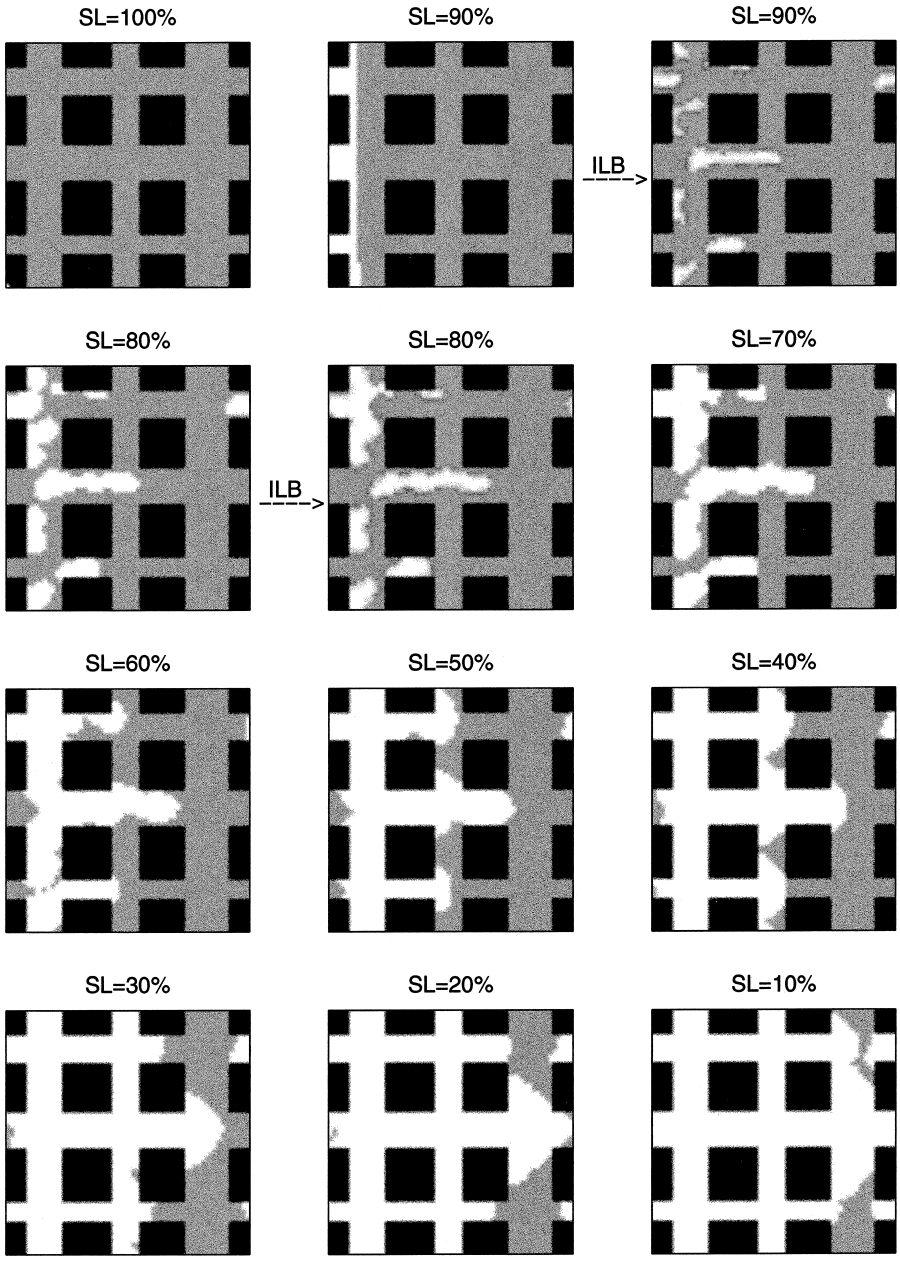

Fig. 15. Phase distribution in the two-dimensional network before the application of the ILB program, i.e. at the beginning of loop 1 where a new phase distribution is proposed (cf. Fig. 3). Data are for: LG, initial composition $z_1{}^\circ = 0.5$; $Q_0 = 25.67$ kg/m^2 s.

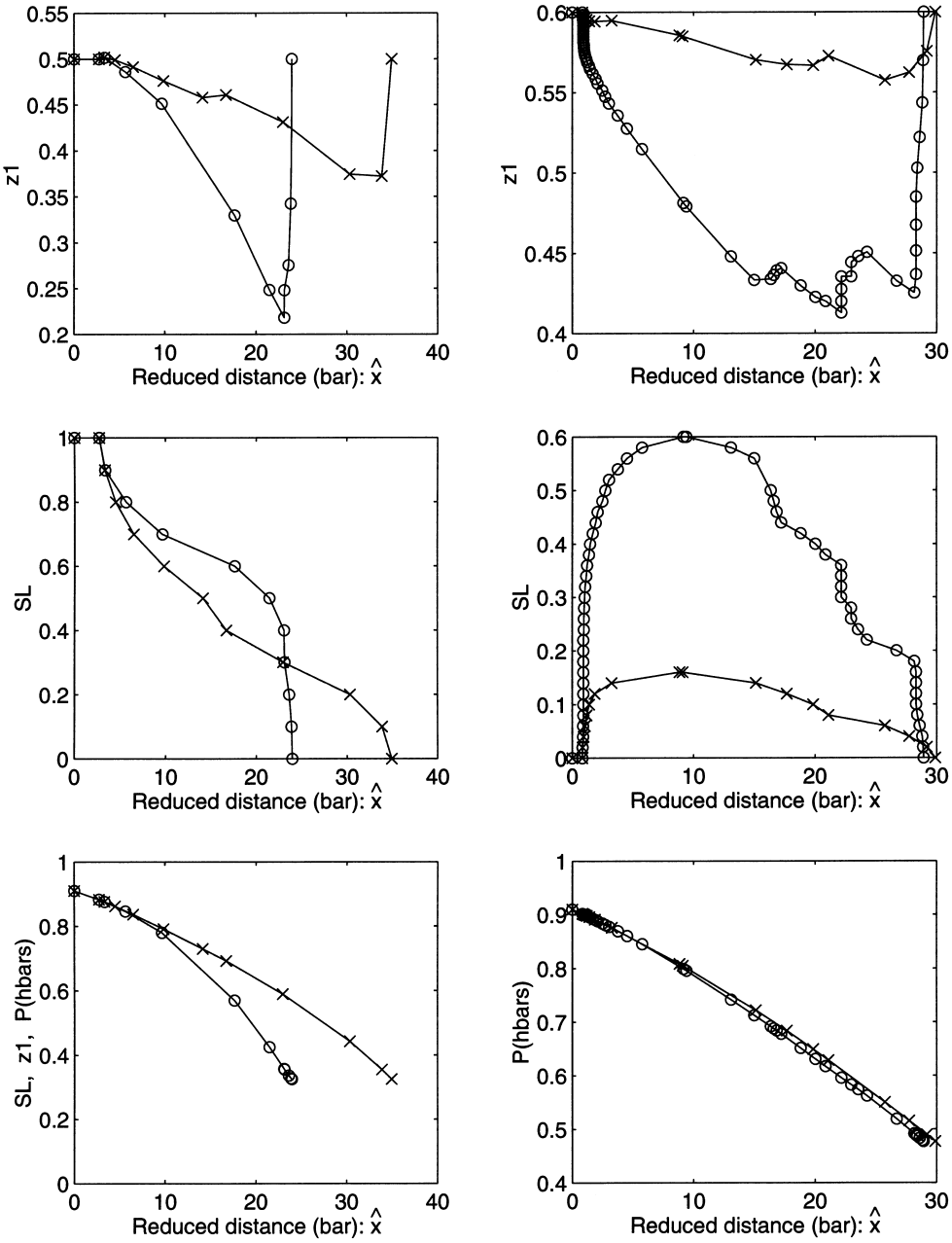

Fig. 16. Evolution of the macroscopic parameters for the two-dimensional network. The left column corresponds to a liquid to gas (LG) evolution, the right column to retrograde condensation (RC). General conditions are given in Table 2. Data are for: ○ ($Q_0 = 2567$ kg/m^2 s), × ($Q_0 = 25.67$ kg/m^2 s).

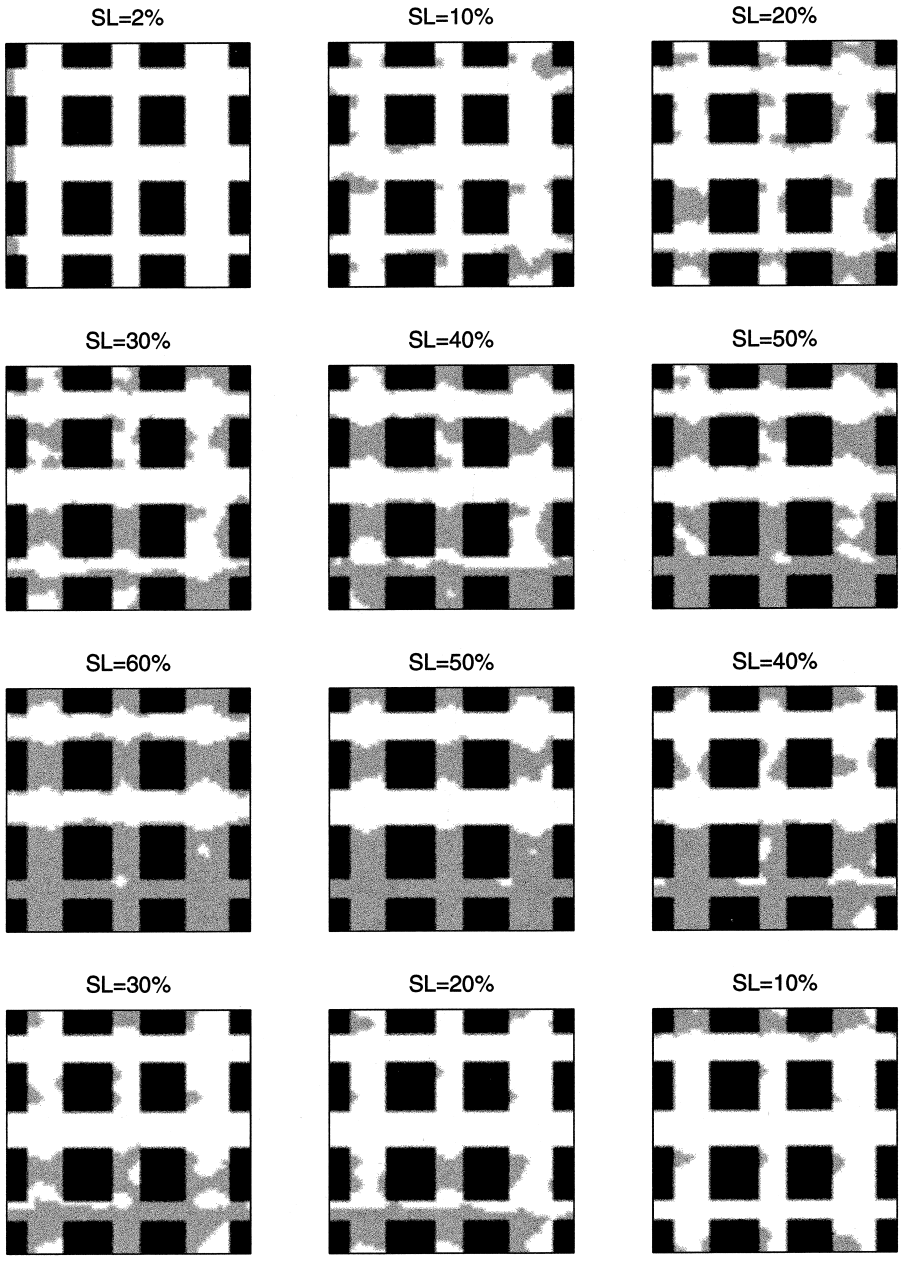

Fig. 17. Phase distribution in the two-dimensional network before the application of the ILB program. Data are for: LG, initial composition $z_1{}^\circ = 0.6$; $Q_0 = 2567$ kg/m^2 s.

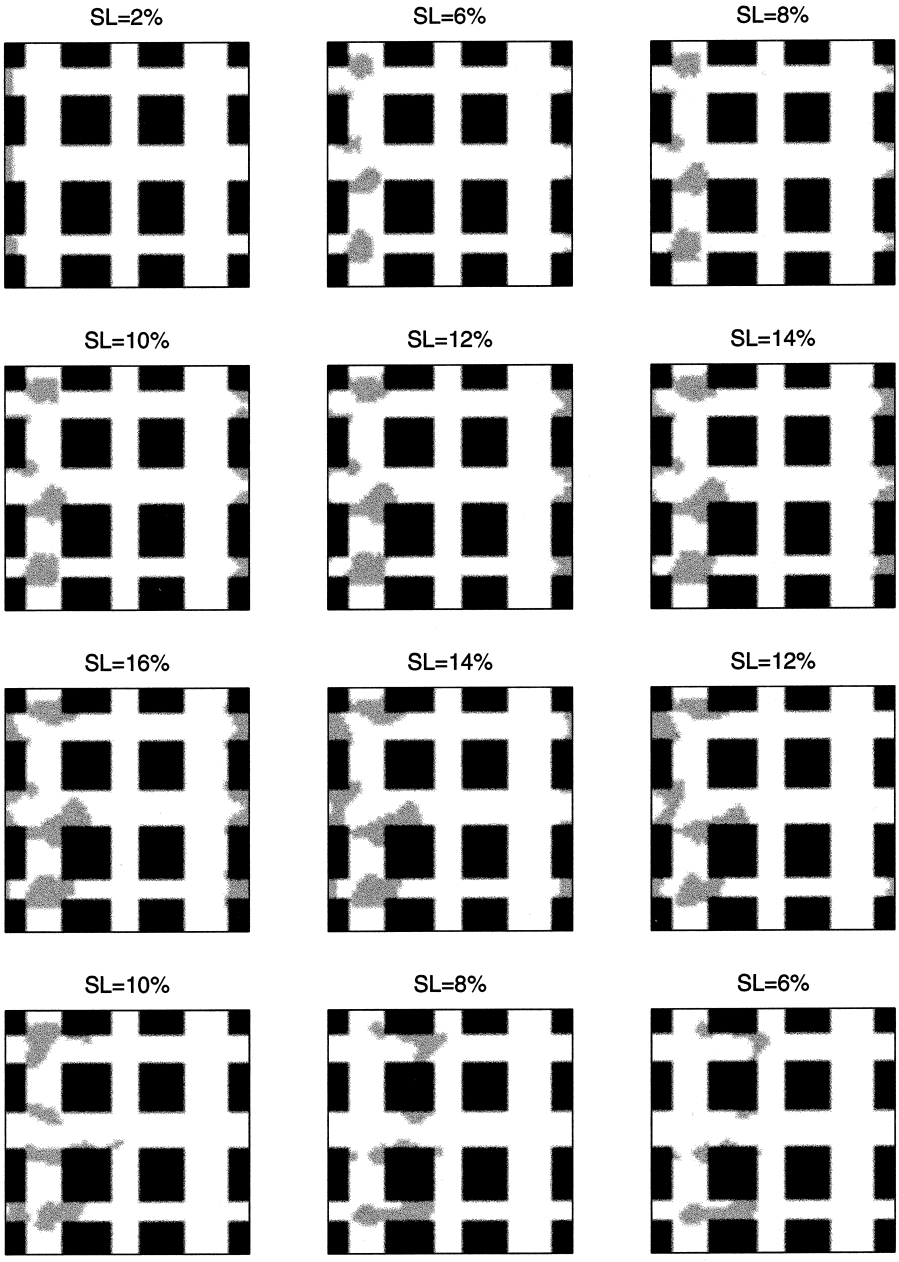

Fig. 18. Phase distribution in the two-dimensional network before the application of the ILB program. Data are for: LG, initial composition $z_1{}^\circ = 0.6$; $Q_0 = 25.67$ kg/m^2 s.

compositions go down as was the case for the constriction with an asymmetry; this may mean that the liquid phase is preferentially created in the low velocity regions. As for saturations, the variations are much larger for large flow rates.

5.3. Reconstructed media

The reconstructed sample corresponds to a Vosges sandstone of porosity $\varepsilon = 0.16$; the unit cell contains 20^3 elementary cubes of size $a = 2.04$ μm; it is represented in Fig. 2(c). It should be noticed that each cube is discretized into eight elementary cubes. Note also that single phase calculations in Adler et al. (1990) were started with precisely the same numbers and that the obtained permeabilities were comparable to the experimental data. This case is the closest one to the real porous media, though the capillary numbers are too high. It might be useful to recall that the flow is only slowly varying and that the fluid is in thermodynamic equilibrium in agreement with Eqs. (1), (33a) and (33b). On an IBM Risk station, it takes about 36 h to complete one step in the loop over saturation in Fig. 3.

For three-dimensional media, it is difficult to get a clear picture of the phase evolution and so only overall quantities will be provided. As for the two-dimensional networks, four cases were investigated with two initial compositions and two flow rates (cf. Table 2). The nucleation problem remains the same as before and it was chosen to create the second phase as a slice perpendicular to the average pressure gradient; again more systematic studies of the influence of the initial phase distributions are needed. In order to give an idea of the precision, two saturation steps $\delta S_L = 0.02$ and 0.1 were systematically used for the LG evolution; it will be seen in Figs. 19–21 that the results are very close one to another; hence, a large saturation step could be used for systematic calculations without a significant loss in precision.

The classical macroscopic results are provided in Fig. 19 for the liquid to gas evolution and the retrograde condensation. Let us start with the liquid to gas evolution; again the dimensionless pressure variations are widely different, but they are still more different if one goes back to the dimensional values. The same comments as for the two-dimensional network also apply in this case; it is remarkable how close the present variations are from the previous case, in the overall behaviour of the curves, but also in the details of the variations with the flow rates. For instance, the evolutions of the composition and of the liquid saturations are very similar.

The evolutions for retrograde condensation are somewhat less important than before. The dimensionless pressure variations for the two flow rates are close, but less close than for the two-dimensional network. However, the evolution of the compositions and of the liquid saturations are also less marked than before.

Note that for both liquid to gas evolution and retrograde condensation, the composition z_1 goes down as for the asymmetric constriction. Again one may think that the second phase is preferentially created in the low velocity regions.

Hence, from the comparison between these two series of curves, it seems that the influence of the flow rate is approximately the same. This is further confirmed by the relative permeabilities which are displayed in Fig. 19. These permeabilities are determined by means of the flow rate of each phase. It is remarkable to see that the liquid permeability K_r^L is strongly decreased when flow is increased both for the liquid to gas evolution and retrograde

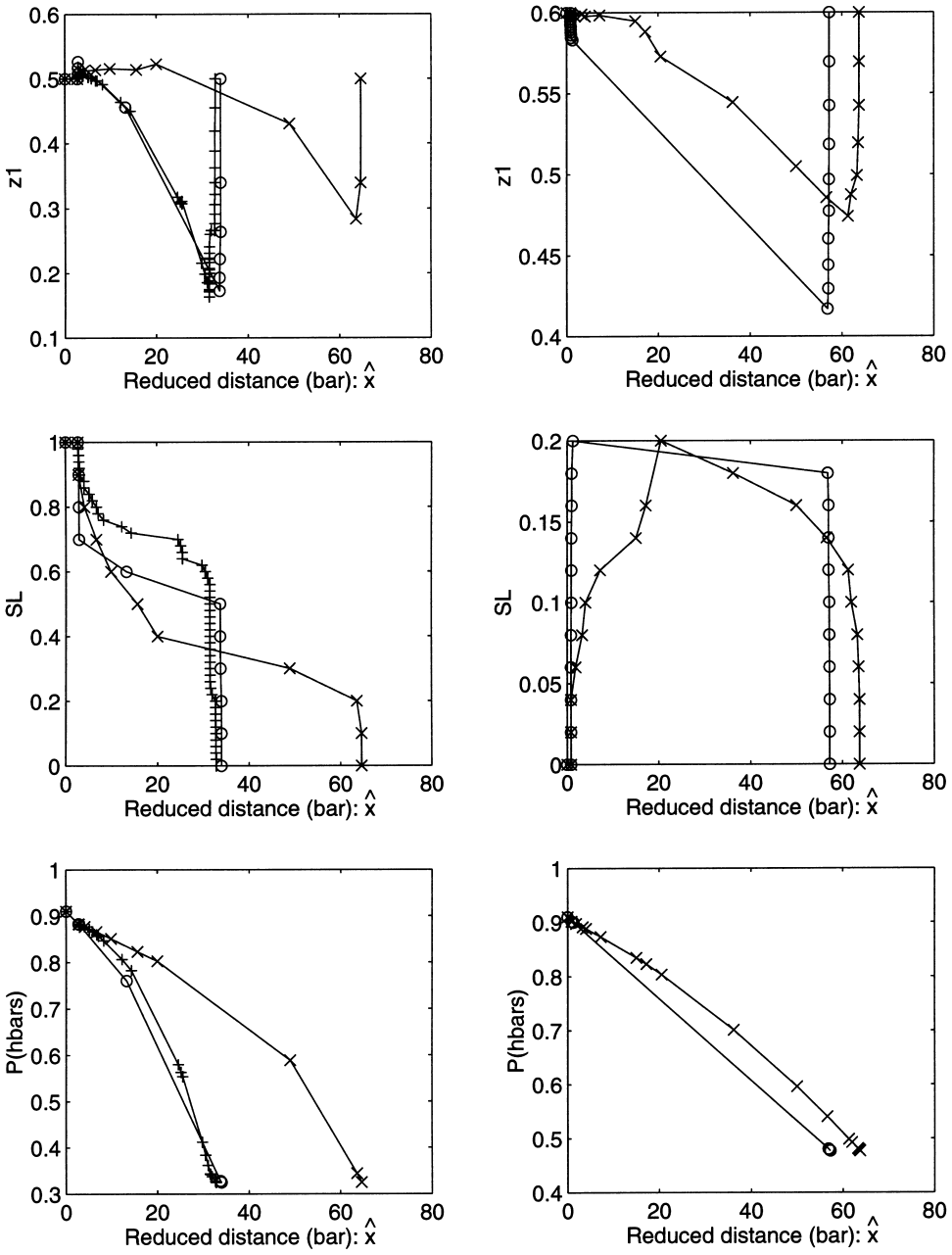

Fig. 19. Evolution of the macroscopic parameters for the reconstructed porous medium. The left column corresponds to a liquid to gas (LG) evolution, the right column to retrograde condensation (RC). General conditions are given in Table 2. Data are for: $Q_0 = 7$ kg/m^2 s (○: $\delta S_L = 0.1$; +: $\delta S_L = 0.02$); $Q_0 = 7$ kg/m^2 s (×).

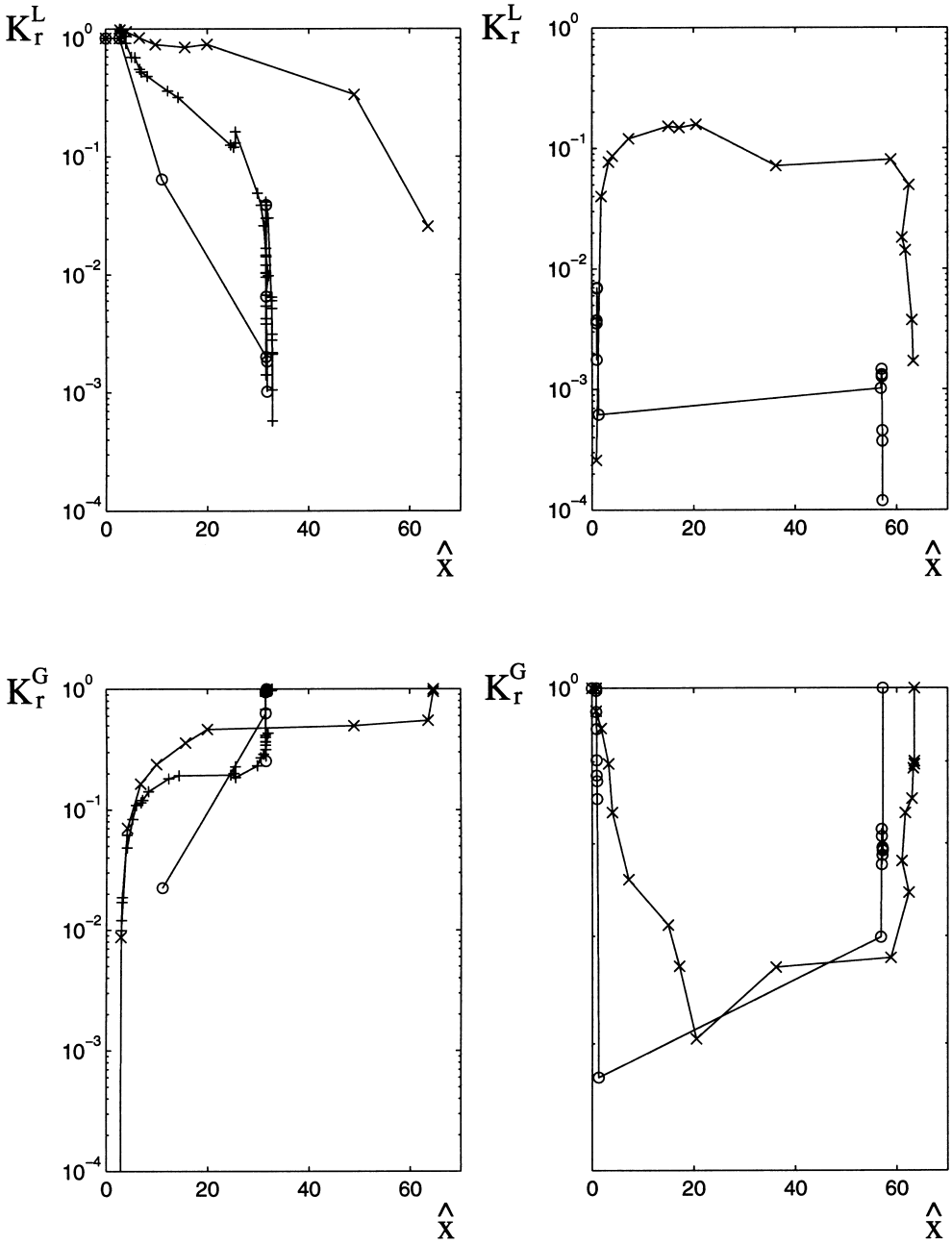

Fig. 20. Evolution of the relative permeabilities for the reconstructed porous medium as functions of the reduced distance $\hat{x}$. The left column corresponds to a liquid to gas (LG) evolution, the right column to retrograde condensation (RC); the first line corresponds to relative liquid permeability, and the second line to relative gas permeability. General conditions are given in Table 2.. Data are for: $Q_0 = 7$ kg/m^2 s (○: $\delta S_L = 0.1$; +: $\delta S_L = 0.02$); $Q_0 = 7$ kg/m^2 s (×).

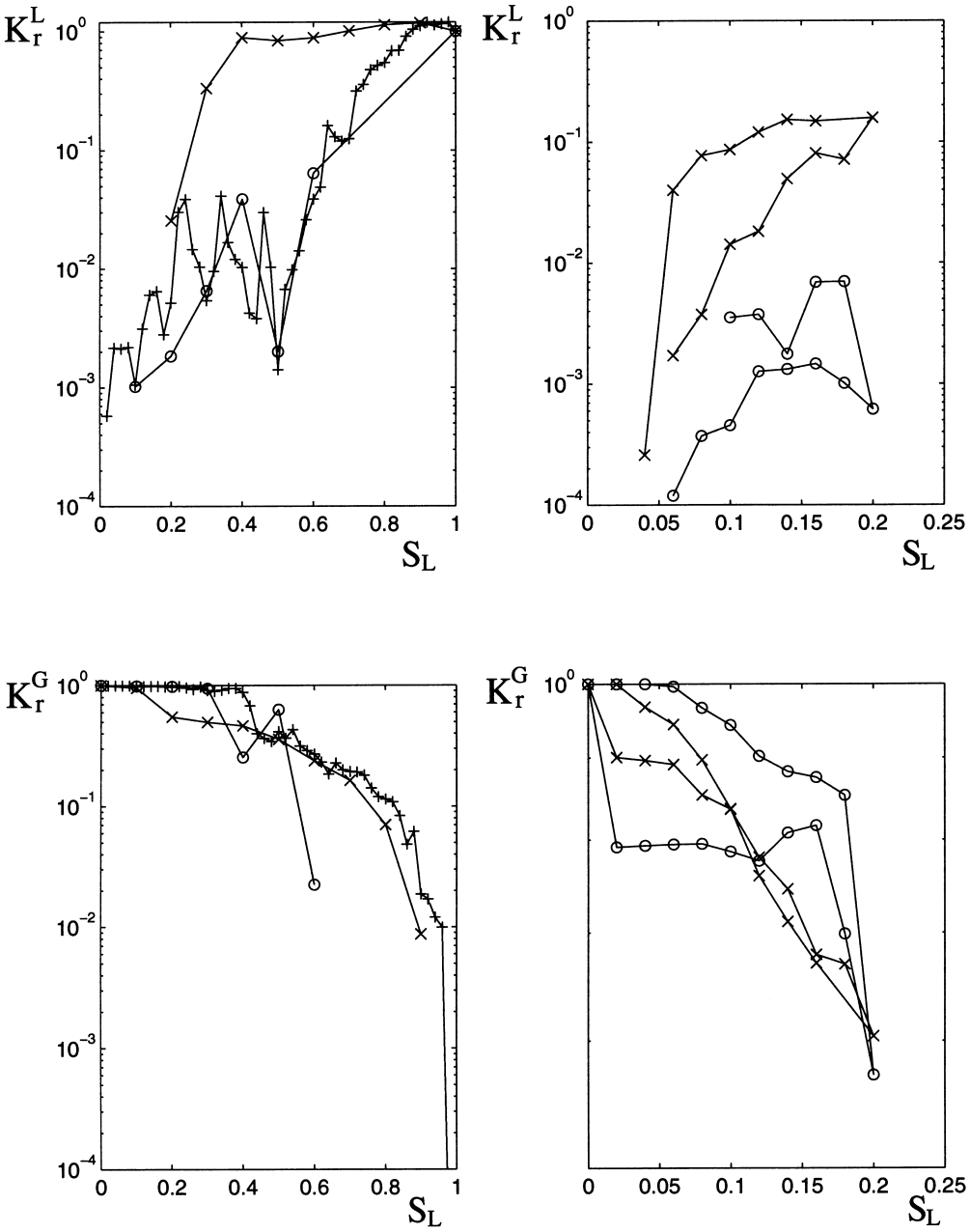

Fig. 21. Evolution of the relative permeabilities for the reconstructed porous medium as a function of liquid saturation S_L. The left column corresponds to a liquid to gas LG evolution, the right column to retrograde condensation RC; the first line corresponds to relative liquid permeability, and the second line to relative gas permeability. General conditions are given in Table 2. Data are for: $Q_0 = 7$ kg/m^2 s (○ $\delta S_L = 0.1$; +:$\delta S_L = 0.02$); $Q_0 = 7$ kg/m^2 s (×).

condensation. When the global flow rate is increased by a factor 100, K_r^L is decreased by approximately two orders of magnitude. This is exactly what was anticipated in Figs. 14, 15, 17 and 18 for two-dimensional networks. Needless to say, when K_r^L is decreased by two orders of magnitude, it can be considered as equal to zero from the experimental point of view.

However, the gas permeability K_r^G has a very different evolution. Its first characteristic is that it remains close to 1 and that it depends much less upon the flow rate than K_r^L.

A different view, perhaps closer to some lab experiments, can also be given in Fig. 21 where the relative permeabilities are plotted as functions of the liquid saturation. Again the role of the flow rate is clear for K_r^L. Nothing really new appears for the liquid to gas evolution. However, it is quite interesting to consider the evolution of K_r^L for retrograde condensation; an hysteresis cycle is created and K_r^L is smaller when the liquid saturation decreases; because of the history of the flow and of the value of the flow rate, the liquid phase is progressively pushed in the dead fluid regions.

6. Concluding remarks

Preliminary results on multicomponent multiphase flows through porous media are given in this paper. In every aspect of the analysis, a great effort has been done to be closer to the practical situations of interest.

This analysis necessarily induces a significant numerical effort. It should be noticed that at the moment, the limiting factor is the length of the computations, rather than the size of the memories.

The present study can be extended in many ways. Variations of important physical parameters such as temperature, nature and number of the components, porous medium and mass flow rates could be systematically investigated. Statistical studies on nucleation sites could also be systematically performed, as well as the influence of the initial phase distribution.

Acknowledgements

This work has been partially supported by a contract of the Institut Français du Pétrole. Most of the computations have been performed at CINES (subsidized by MENRT) at Montpellier.

References

Adler, P.M., 1992. Porous Media: Geometry and Transports. Butterworth/Heinemann, London.

Adler, P.M., Jacquin, C.G., Quibier, J.A., 1990. Flow in simulated porous media. Int. J. Multiphase Flow 16, 691–712.

Appert, C., Zaleski, S., 1990. A lattice gas with a liquid–gas transition. Phys. Rev. Lett. 64, 1–4.

Atkin, R.J., Craine, R.F., 1976a. Continuum theories of mixtures : basic theory and historical development. Q. J. Mech. and Appl. Mathematics 29, 207–244.

Atkin, R.J., Craine, R.F., 1976b. Continuum theories of mixtures : applications. J. Inst. Math. Appl. 17, 153.

D'Humières, D., Lallement, P., Frisch, U., 1986. Lattice gas models for 3D hydrodynamics. Europhysics Letters 2, 291–297.

Du, C., Yortsos, Y.C., 1999. A numerical study of the critical gas saturation in a porous medium. Transport Porous Media 35, 205–225.

El Yousfi, A., Zarcone, C., Bories, S., Lenormand, R., 1991. Mécanismes de formation d'une phase gazeuse par détente d'un liquide en milieu poreux. C. R. Acad. Sci. Paris 313 (II), 1093–1098.

Frisch, U., Hasslacher, B., Pomeau, Y., 1986. Lattice-gas automata for the Navier–Stokes equations. Phys. Rev. Lett. 56, 1505–1508.

Frisch, U., d'Humières, D., Hasslacher, B., Lallemand, P., Pomeau, Y., Rivet, J.P., 1987. Lattice gas hydrodynamics in two and three dimensions. Complex Systems 1, 649–707.

Geilikman, M.B., Dusseaut, M.B., 1999. Sand production caused by foamy oil flow. Transport Porous Media 35, 259–272.

Ginzbourg, I., Adler, P.M., 1995. Surface tension models with different viscosities. Transport Porous Media 20, 37–76.

Gravier, J.F., 1986. Propriétés des fluides de gisements, Tome 2, Technip Editions.

Gustensen, A.K., 1992. Lattice-Boltzmann studies of multiphase flow through porous media. Ph.D. Thesis, MIT Press.

Hayes, R.E., Maini, B.B., 1999. Foamy oil flow in porous media. Transport Porous Media 35.

Higuera, F.J., Jimenez, J., 1989. Boltzmann approach to lattice gas simulations. Europhysics Letters 9, 663–668.

Li, X., Yortsos, Y.C., 1995. Visualisation and simulation of bubble growth in pore networks. AIChE J. 41, 214–222.

McNamara, G.R., Zanetti, G., 1988. Use of the Boltzmann equation to simulate lattice-gas automata. Phys. Rev. Lett. 61, 2332–2335.

Reid, R.C., Prausnitz, J.M., Poling, B.E., 1987. The Properties of Gases and Liquids, 4th ed. McGraw-Hill, New York.

Sheng, J.J., Maini, B.B., Hayes, R.E., Tortike, W.S., 1999. Critical review of foamy oil flow. Transport Porous Media 35, 157–187.

Succi, S., Foti, E., Higuera, F., 1989. Three-dimensional flows in complex geometries with the lattice Boltzmann method. Europhysics Letters 10, 433–438.